Durham E-Theses

Designing the detection system for the CORUS project

KALOGIROU, ANGELIKI

How to cite:

Use policy

Designing the detection system for the CORUS project

Angeliki Kalogirou

A thesis submitted to the University of Durham

in accordance with the regulations for admittance

to the Degree of Master in Science

Very High Energy Gamma-Ray Group

Department of Physics

Durham Univerisy

May 2013

Abstract

CORUS (Cosmic Rays in UK Schools) will be a network of muon detectors based in schools across the UK. Networks similar to CORUS already exist in other countries, such as the Netherlands and USA. The main aim of the project is to teach high schools students about cosmic rays and experimental physics as well as to motivate them to pursue studies in science. A set of muon detectors will be used for this purpose and the objective of this study is to complete the design of the detectors, construct them and test their capabilities and limitations.

The most important component of the muon detector is the electronic card used to collect, analyse and output data. A DAQ card used by QuarkNet, a network of detectors in the USA, has been used in the design of the CORUS detectors. Some readily available photomultiplier tubes have also been used, along with an interface board which connects them to the DAQ board. In this study, I tested whether these two components work well together by conducting a series of experiments, intended to be performed by the students, with the final detector set-up. The end result is that although a number of improvements is needed before the detectors serve their purpose, this particular set-up does not impose any limitations to the experiments that it is intended to be used for.

Contents

i

Declaration

I declare that no material presented in this thesis has been previously submitted by myself for a degree at this or any other university.

Acknowledgements

I would like to thank my supervisor Dr. Paula Chadwick for her guidance, her valuable feedback and her support through the course of this work.

Chapter 1

An Introduction to Cosmic Rays

1.1 Introduction

The year 2012 marked the centenary of the discovery of cosmic rays, a crucial step in the development of modern physics. Cosmic rays were discovered in 1912 by Victor Hess [1], while he was trying to find the source of background radiation, which was thought to come from the Earth's crust and expected to decrease with altitude. He greatly increased the precision of the instruments (electroscopes) and took them on balloon flights himself. For one year (1911-12) he measured the level of radiation at altitudes up to 5.2 km and he found out that it decreased up to an altitude of about 1 km, but above that it increased considerably, with the radiation detected at 5 km about twice that at sea level. He explained the phenomenon with the hypothesis that there is a source of radiation coming into the Earth's atmosphere from above. For his discovery he

received the Nobel prize in 1936.

In this chapter I will describe the basic physics behind cosmic rays focusing on how cosmic rays and especially muons propagate in the atmosphere. Lastly, I will present the calculations I made in order to find the expected muon flux at sea level.

1.2   Abundances and Energy Spectrum

Cosmic rays are charged particles, reaching the Earth's atmosphere from space at a rate of about 1000 per square meter per second. As observed at the top of the atmosphere, about 90% of the particles are protons, 9% alpha particles and the rest heavier nuclei [2].

Figure 1.2.1 shows the relative abundances of cosmic rays compared to the abundances of elements in the solar system. Both solar system and cosmic ray abundances show the odd/even effect (elements with even atomic number Z are more tightly bound and as a result they are more abundant). There are two differences between the two compositions.

First, there is an under-abundance of hydrogen and helium in cosmic rays compared to the solar system. This is not completely understood but it might have to do with a rigidity cutoff or deceleration at the boundaries of astrospheres and interstellar space [4].
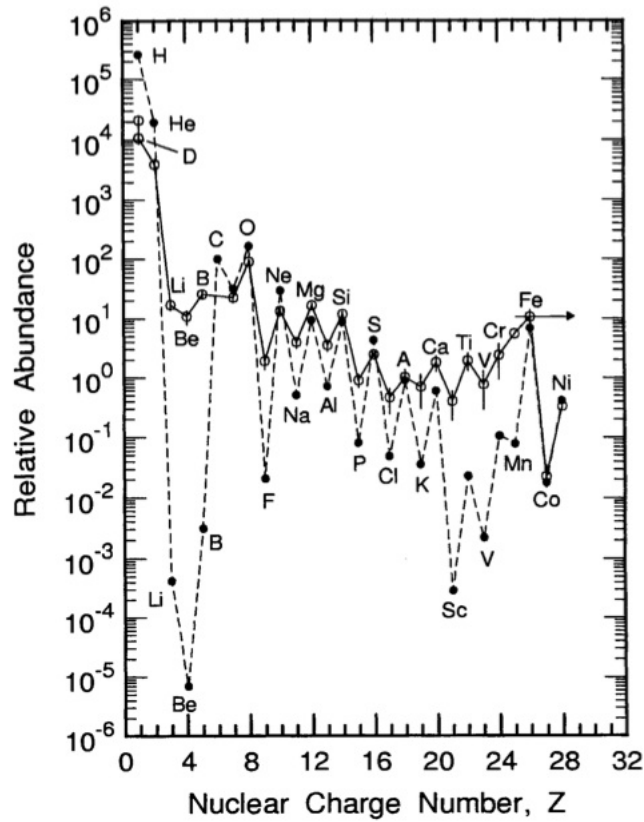
Figure 1.2.1: Abundances of elements in cosmic rays (white circles) and in the solar system (black circles) relative to carbon [3].

Second, there are two groups of elements, (Li, Be, B and Sc, Ti, V, Cr, Mn) that are many orders of magnitude more abundant in the cosmic radiation than in the solar system. The reason for this is that these elements are not in fact end products of the stellar nucleosynthesis; they are detected in cosmic rays as the spallation products of the abundant nuclei of carbon and oxygen (Li, Be, B) and of iron (Sc, Ti, V, Cr, Mn) [2].

Figure 1.2.2 shows the differential energy spectra for protons, helium, carbon, oxygen and iron nuclei as a function of the kinetic energy per nucleon of the particles.

3
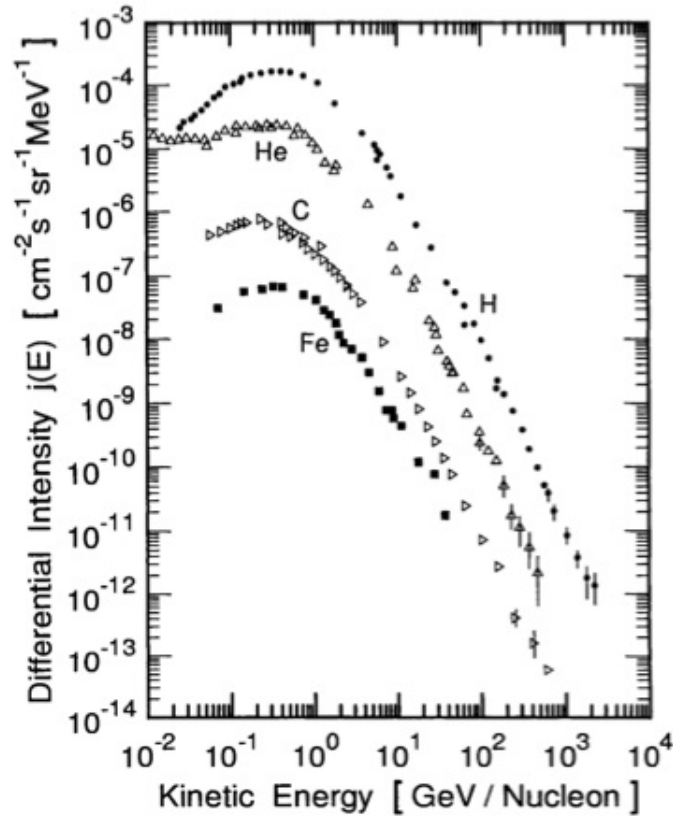
Figure 1.2.2: The differential energy spectra of different cosmic ray species [3].

The spectra exhibit a power-law behaviour at energies over 1 GeV per nucleon. At lower energies there is a cut-off due to a phenomenon called solar modulation. During periods of high solar activity the flux of low energy cosmic rays is decreased, with a maximum observed during phases of low solar activity. The reason for this phenomenon is that the particles diffuse in towards Earth from interstellar space through the outflowing solar wind. The greater the solar activity, the greater the solar disturbances in the interplanetary magnetic field which impede the propagation of particles with energies less than about 1 GeV per nucleon to the Earth. The solar minimum and maximum cycle is 11 years.

The energy spectra of cosmic rays with energies in the range $10^9 - 10^{14}$ eV exhibit a power-law behaviour. It can be described by the equation:

$$N(E)dE = KE^{-x}dE \qquad (1.2.1)$$

with $x \approx 2.5 - 2.7$. The spectrum is characterised by some features as the "knee" at 10^{15} eV where the spectrum steepens and x approaches 3, and the "ankle" at 10^{18} eV, where the spectrum flattens and x becomes about 2.7 again (Fig. 1.2.3).

It has been suggested that there is a cutoff in the primary cosmic ray spectrum around 10^{20} eV called the "GZK" cutoff, predicted by Greisen [5] and Zatsepin and Kuzmin [6]. The cutoff is a result of the interaction of extragalactic cosmic rays with the cosmic microwave background radiation which causes the cosmic rays to lose their energy. Latest experimental data from the Pierre Auger Observatory seem to validate this prediction [7]. More details can be found in section 2.2.4.

The intensity I_N of primary nucleons in the energy range from several GeV to over 100 TeV is given approximately by:

$$I_N(E) \approx 1.8 \times 10^4 \, E^{-2.7} \text{nucleons m}^{-2}\text{s}^{-1}\text{sr}^{-1}\text{GeV}^{-1} \qquad (1.2.2)$$

where E is the energy per nucleon in GeV.
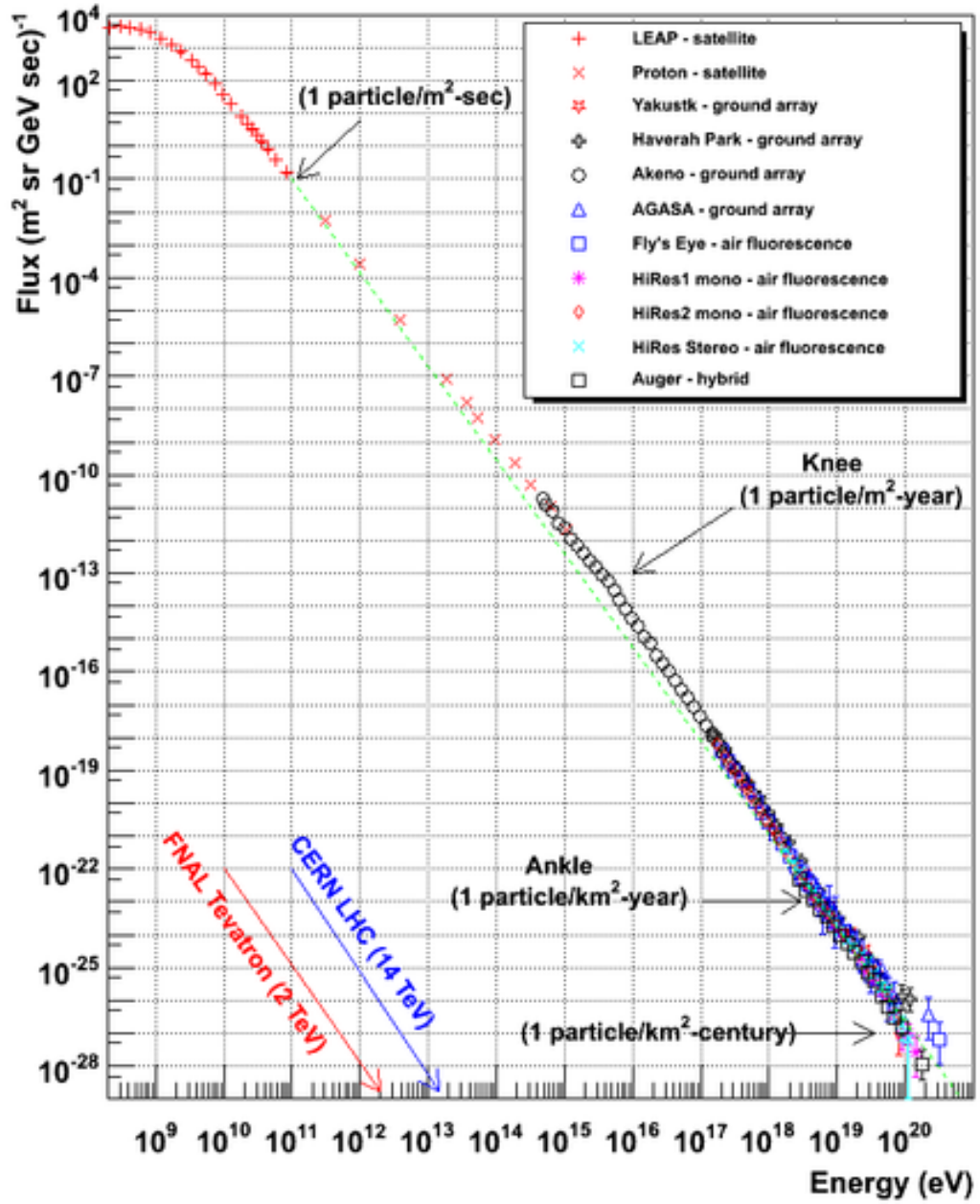
Figure 1.2.3: The differential energy spectrum of cosmic rays from various experiments [8] (updated image from [9]).

The two fundamental questions about cosmic rays are where they come from and how they are accelerated to such high energies. The bulk of cosmic rays are of Galactic origin, but the high energy tail, with energies over 10^{19} eV, is probably of extragalactic origin. Their exact origin is still a matter of debate. Various objects in our Galaxy can act as particle injectors and different acceleration mechanisms are able to accelerate or possibly reaccelerate cosmic rays to energies of about 10^{15} or 10^{16} eV, some even to 10^{18} eV. The prime candidates for the acceleration of cosmic rays in the Galaxy are supernova remnants in which the particles bounce back and forth in the shock front of the remnant, gaining energy until they have enough to escape. However, the origin of particles with energies beyond the limit of 10^{18} eV is harder to explain, though various more or less exotic models and processes have been proposed. For example, it has been suggested that cosmic rays are generated in gamma ray bursts [10], [11], [12], in the cores of active galactic nuclei [13] or by cosmic strings [14].

1.3 Isotropy and Energy Density

Figure 1.3.1 shows the anisotropy in the distribution of arrival directions of cosmic rays as a function of energy. The arrival directions of cosmic rays of energies in the range $10^{13} - 10^{14}$ eV are remarkably uniform, with anisotropy less than 1 part in 10^3.
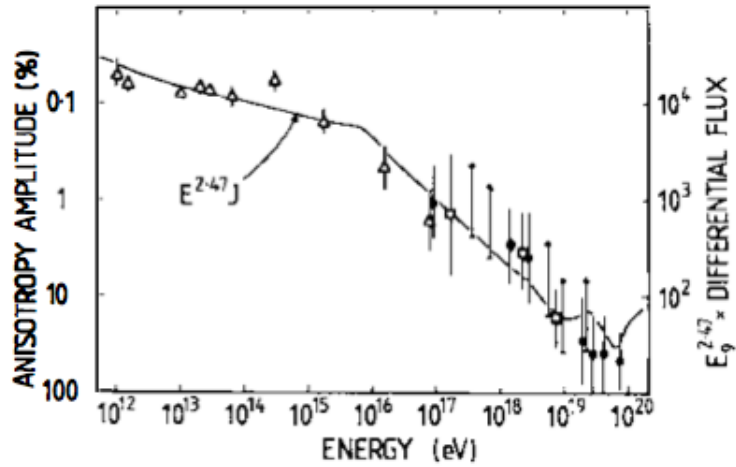
Figure 1.3.1: The amplitude of the anisotropy in the distribution of arrival directions of cosmic rays. The solid line represents the differential spectrum of cosmic rays [15].

Only the highest energy protons and nuclei reach the Earth without being deflected by the magnetic field in the interplanetary medium. The gyroradius of a relativistic proton is:

$$r_g = 3 \times 10^9 \; \gamma \; (B/10^{-9}T) \; m \qquad (1.3.1)$$

where the magnetic field strength B is measured in Tesla and γ is the Lorentz factor. The local magnetic field strength in the interplanetary medium is B = 10^{-9} T, so relativistic protons with $\gamma = 10^3$ (corresponding to energies of 10^{12} eV) have gyroradii of 3×10^{12} m = 20 AU, which is roughly the radius of the orbit of Uranus. Thus, only particles with energies greater than this are likely to preserve information about their arrival direction when they arrive at the top of the Earth's atmosphere.

If we assume that the flux of high energy particles at the top of the atmosphere is representative of that present in the local interstellar

8

medium, we can estimate a lower limit for the local energy density in high energy particles. Very high energy cosmic rays (with energy greater than 10^{15} eV) don't contribute significantly in this density because they are very rare. The maximum of the observed proton spectrum corresponds to about 2 protons $m^{-2}s^{-1}sr^{-1}$ MeV^{-1} at an energy of about 1 GeV. The total energy density of cosmic rays with energies greater than 1 GeV is about 1 MeV m^{-3} [16].

1.4   Cosmic Rays in the Atmosphere

When high energy cosmic ray protons and nuclei enter Earth's atmosphere, they initiate nucleonic cascades. The incoming cosmic ray particles are called the primary particles and the particles that are created from these cascades are called the secondary particles. The secondary particle spectra exhibit the same power-law form of the primary spectrum, with a very similar exponent. What follows is a basic description; more detailed information can be found in [3] from which much of the following is derived.

There are three major extensive air shower components: the hadronic, the electromagnetic and the muon component (Fig.1.4.1). Another classification is based on the penetration ability of particles, dividing them into the hard component, composed mainly of energetic hadrons and muons, and the soft component, composed of electrons and low energy muons. At sea level the hard component consists mostly of muons. In addition, there is a neutrino component, but because of the small neutrino cross section, detection above ground is extremely difficult.

Figure 1.4.1: Schematic diagram of a nucleonic cascade in the atmosphere [3].

A high energy proton undergoes on average 12 interactions before reaching the Earth's surface (at sea level) following a vertical trajectory. This means that the interaction mean free path λ_i is about 80 g cm^{-2}. The heavy nuclei of the primary radiation don't reach the Earth's surface without being fragmented because their interaction mean free path λ_i is

about 23 g cm^{-2} corresponding to about 50 interactions for a vertical trajectory through the atmosphere.
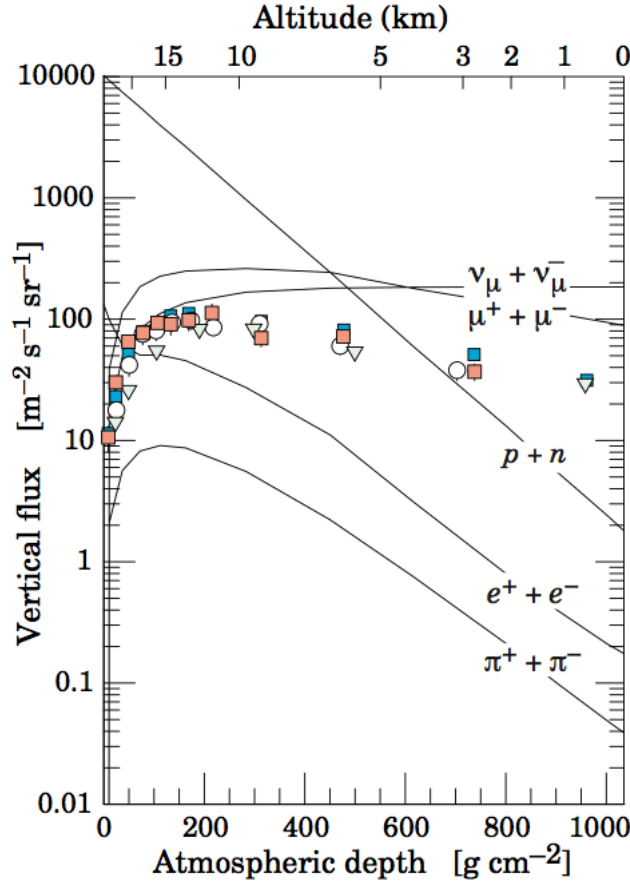
Figure 1.4.2: The vertical fluxes of different components of cosmic rays with energies more than 1 GeV in the atmosphere. The points show measurements of negative muons [17].

Figure 1.4.2 shows the distribution of the products of the nucleonic cascades in the atmosphere. The majority of the observed flux is caused by primary protons with energies over 1 GeV. The path length for interaction of these protons with the atmospheric atoms and molecules is about 800 kg m^{-3}, compared with the total depth of about 10,000 kg m^{-3}. This explains the rapid rise in the fluxes of all the cascade products at the top of the atmosphere. The proton flux then falls expo-

nentially with path length and neutron and pion fluxes fall exponentially as well. The number of electrons and positrons grows exponentially at first due to electron-photon cascades and then drops rapidly. The high energy muon flux falls slowly, but the low energy muons don't reach the surface of the Earth.

When a high energy proton encounters an atmospheric nucleus, it will interact strongly with an individual nucleon in the nucleus, producing pions of all charges (π^+, π^-, π^0). Strange particles, such as kaons, other mesons and hyperons may also be produced and occasionally antinucleons as well. If the secondary nucleon and charged pions have enough energy, they will continue to multiply through successive generations of nuclear interactions until the energy per nucleon drops below that required for pion production (about 1 GeV). The initial energy of the nucleon is shared among the pions, strange particles and anti nucleons, a process called pionisation. Unstable particles such as pions, kaons and others are also subject to decay. Which process will be followed depends on the mean life and energy of the particle and on the density of the medium in which they propagate. For a given particle in the atmosphere the probabilities for the two processes depend on the energy, altitude and zenith angle.

The neutral pions have short lifetimes of 1.78×10^{-16} s before decaying into two γ-rays, each of which initiates an electromagnetic cascade. An electromagnetic cascade is the process by which a high energy photon in the upper atmosphere, with energy of at least 1 MeV, generates an electron-positron pair, each of which in turn generates high energy photons by Bremsstrahlung and so on. This process leads to extensive

air showers. The millions of secondaries created are scattered laterally from the central axis of the cascade as a result of the transverse momenta acquired at creation and due to scattering processes.

The charged pions have a lifetime of 2.6×10^{-8} s and an interaction mean free path of about 120 g cm^{-2}. Many of the charged pions decay into muons releasing muon neutrinos and antineutrinos:

$$\pi^+ \rightarrow \mu^+ + \nu_\mu$$
$$\pi^- \rightarrow \mu^- + \overline{\nu}_\mu$$

(1.4.1)

The low energy muons decay into positrons, electrons and muon neutrinos with a lifetime of 2.2×10^{-6} s:

$$\mu^+ \rightarrow e^+ + \nu_e + \overline{\nu}_\mu$$
$$\mu^- \rightarrow e^- + \overline{\nu}_e + \nu_\mu$$

(1.4.2)
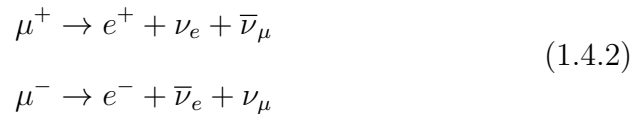
If the primary particle has high enough energy, then the muons produced have very high energy and are highly penetrating. Since their ionisation losses are small and they have no nuclear interactions they can be observed at the surface of the Earth. Their lifetime is 2.2×10^{-6} s in their rest reference frame but since they are relativistic their lifetime in the reference frame of the external observer is 4.1×10^{-4} s. This time is enough for them, since they need about 10^{-4} s to reach the surface of the Earth. In addition, the high energy muons can penetrate quite far underground thus providing an effective means of monitoring the average intensity and isotropy of the flux of cosmic rays arriving at the top of the atmosphere.

1.4.1   Muons in the Atmosphere

As has been described above, muons are the products of the decay of charged pions and to a much lesser extent of charged kaons. At very high energies, in the TeV range, a small contribution arises from the decay of charmed particles, such as D-mesons and other, massive particles.

The decay probability for muons W_μ is given by the following formula:

$$W_\mu \simeq \frac{m_0 X \sec(\theta)}{\rho \tau_0 p} \tag{1.4.3}$$

where $m_0 [\mathrm{GeV}/c^2]$ is the rest mass of the particle, $X[\mathrm{g\ cm}^{-2}]$ the thickness traversed, $\tau_0[\mathrm{s}]$ the mean life of the particle, $\rho[\mathrm{g\ cm}^{-3}]$ the density, θ the zenith angle and $p[\mathrm{GeV}/c]$ the momentum. The corresponding survival probability is:

$$S_\mu = (1 - W_\mu) \tag{1.4.4}$$

Figure 1.4.3 shows the survival probability for muons originating from an atmospheric depth of 100 g cm^{-2}.
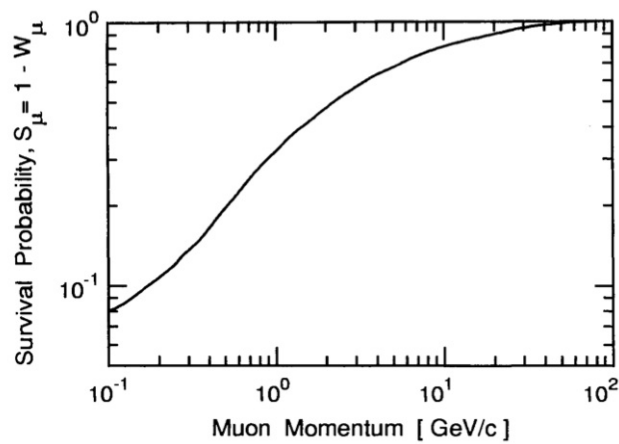
Figure 1.4.3: Survival probability of muons originating from an atmospheric depth of 100 g cm^{-2} to reach sea level versus muon momentum [3].

14

The differential energy spectrum of muons (Fig.1.4.4) at a specific level in the atmosphere is given by:

$$j_\mu(E) = A_\pi W_\pi (E + \Delta E)^{-\gamma_\mu} (1 - W_\mu) \qquad (1.4.5)$$

where γ_μ is approximately the same as the exponent of the primary spectrum, A_π the normalisation constant for absolute intensity, ΔE the energy loss by ionisation and W_π the pion decay probability.

Figure 1.4.4: Muon differential spectrum compared with the parent pion differential spectrum [3].

Pions in the atmosphere decay or lose energy through interactions. The competition between the two processes depends on the mean life and energy of the pions and on the energy of the medium. For constant

15

density, as the energy increases, more and more pions interact because time dilation reduces the probability for decay. This increases with increasing density. This is the reason why there is a steepening in the muon spectrum compared to the pion spectrum above a certain energy (Fig.1.4.4).

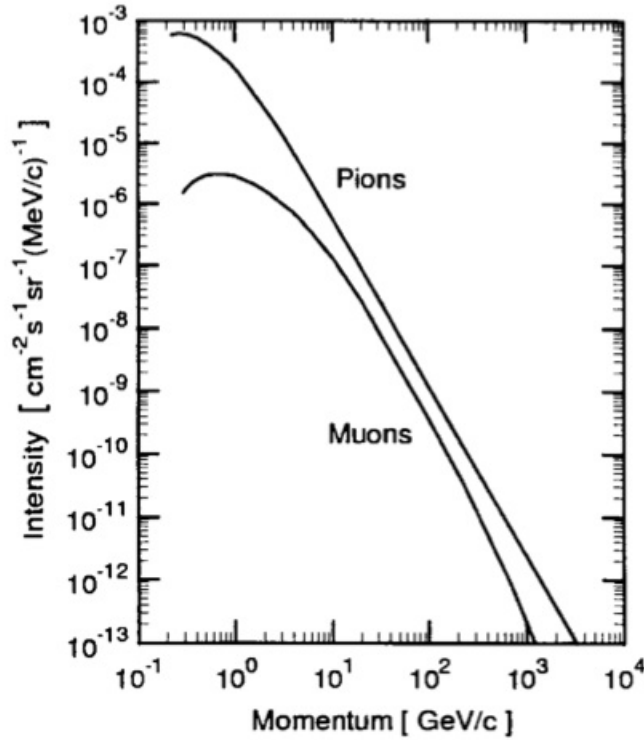Low energy mesons always decay into muons, which subsequently decay while losing energy at a rate that increases as their energy decreases. The result is a maximum in the muon spectrum (Fig.1.4.4).

1.4.2   Muons at Sea Level

Muons are the most abundant secondary particles at sea level, with the exception of photons and neutrinos. The vertical muon intensity at sea level, at low momenta ($p \leq 5$ GeV/c) depends on the geomagnetic latitude λ of the location of the measurement and on the solar activity.

The vertical absolute integral intensity of muons at sea level has been measured to be [18]:

$$I_v(\geq 0.320 \text{ GeV/c}) = (8.4 \pm 0.2) \times 10^{-3} \text{cm}^{-2}\text{s}^{-1}\text{sr}^{-1} \qquad (1.4.6)$$

at geomagnetic latitude 55°N with cut-off rigidity $P_c = 2.2$ GeV. The Physics Department in Durham is at 55°N as well with an altitude of approximately 61 m above sea level so we expect the same value for intensity.

The experimental zenith angle dependence of the muon intensity at

$\theta \leq 75°N$ can be described by the expression [19], [20]:

$$I(\theta) = I(0°)\cos^n(\theta) \qquad (1.4.7)$$

where n is a function of momentum, $n = n(p)$. Its value at latitude 53°N for momentum threshold of 0.35 GeV is [21]:

$$n = 2.16 \pm 0.01 \qquad (1.4.8)$$

In order to calculate the muon flux we integrate the intensity with respect to all solid angles so we get the following integral:

$$J = \int_\Omega I(\theta, \phi)\cos(\theta)\, d\Omega = \int_0^{2\pi} \int_0^{75°} I_v \cos^n(\theta)\cos(\theta)\sin(\theta)d\theta\, d\phi \quad (1.4.9)$$

The result is $J = (1.26 \pm 0.02) \times 10^{-2} \mathrm{cm}^{-2}\mathrm{s}^{-1}$.

The Bethe-Bloch formula [22], [23], [24], [25], [26] gives the energy loss, dE/dx, due to ionization and atomic exitation of a moderately relativistic particle with charge ze in matter with atomic number Z and atomic weight A [27]:

$$-\left(\frac{dE}{dx}\right) = 4\pi N_A r_e^2 m_e c^2 z^2 \frac{Z}{A}\frac{1}{\beta^2}\left[\ln\left(\frac{2m_e c^2 \gamma^2 \beta^2}{I}\right) - \beta^2 - \frac{\delta}{2}\right] \quad (1.4.10)$$

where m_e is the rest mass of the electron, r_e the classical radius of the electron and N_A Avogadro's number, γ is the Lorentz factor and $\beta = v/c$. I is the ionization constant and is approximately given by 16 $Z^{0.9}$ eV for $Z > 1$, and dx is the column density expressed in mass per unit area [g cm^{-2}]. δ represents the density effect which approaches $2\ln\gamma$ plus

17

a constant for very energetic particles [28], [29]. For a singly charged relativistic particle traversing the atmosphere in vertical direction ($\simeq$ 1030 g cm^{-2}) the energy loss is 2.2 GeV.

1.5 Conclusions

This brief introduction covers the basic principles of cosmic ray physics and provides the necessary background information about how muons behave when they reach the Earth. In the next chapters this information is needed to understand and predict results from the experiments conducted but first I will present some of the most important large scale experiments designed to study cosmic rays and their results.

Chapter 2

Cosmic Ray Experiments

2.1 Introduction

In the following chapter I will present the most important modern experiments researching cosmic rays. In the first half I will talk about the research ground arrays. They are large scale experiments based on international collaborations, studying high energy cosmic rays (over 10^{14} eV). Some of the results were contradictory and they are still the subject of scientific research. In the second half of the chapter I will look at existing school arrays dedicated mostly to educate high school students and I will present the philosophy behind the CORUS (Cosmic Rays in Uk Schools) project.

2.2 Research ground arrays

For air showers generated by primary particles with energies over 10^{15} eV there are sufficient particles in the cascade such that the remnant of

the shower can be detected as a correlated event by an array of individual particle detectors on the ground. The threshold (the lowest energy detectable by an instrument) of such a ground array depends on the altitude of the array. Typically it is difficult to measure cosmic rays with energies below 10^{14} eV with ground arrays. The footprint of air showers typically extends hundreds of meters. By measuring the time of arrival of the shower front at the individual stations, the direction of the primary cosmic rays can be calculated.

Some of the most important ground arrays are AGASA (Akeno Giant Air Shower Array), HiRes (High Resolution Fly's Eye), the Yakutsk Extensive Air Shower Array and the Pierre Auger Observatory. Below I describe them briefly and I compare their results. The most important area of research concerns the GZK cutoff mentioned in chapter 1. Figure 2.2.1 is used for comparison of the results on the spectrum of primary cosmic rays from the experiments discussed in this chapter. AGASA reported no evidence of the cutoff [30], whereas HiRes [31] and Yakutsk [32] did. These contradictory results led to the creation of another ground array dedicated to studying high energy cosmic rays, the Pierre Auger Observatory, which has confirmed the presence of the cutoff [33].
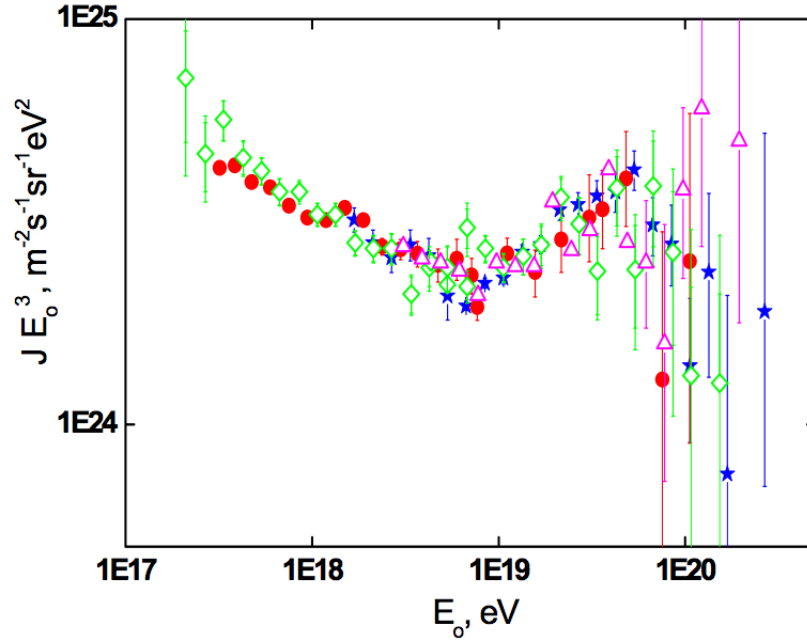
Figure 2.2.1: Comparison of the results of the Yakutsk array (red circles) with AGASA (purple triangles), Auger (blue stars) and HiRes (green rhombuses) [34].

2.2.1 AGASA

AGASA (Akeno Giant Air Shower Array) was a very large array in the Akeno Obsevatory in Tokyo, Japan, that started operating in 1992 and it stopped in 2004. It was dedicated to studying the origin of extremely high energy cosmic rays, with energies over 10^{18} eV. AGASA covered an area of about 100 km^2 and consisted of 111 detectors on the ground (surface detectors) and 27 detectors under absorbers (muon detectors). Each surface detector was placed 1 km away from its nearest neighbour and the detectors were connected with a pair of optical fibres. Basic information about AGASA can be found on the experiment's website [35].

The most important results from AGASA are summarised below:

21

1. In 1993 a cosmic ray of energy 2×10^{20} eV was detected [36]. This is the second highest energy event ever observed.

2. The energy spectrum (Fig.2.2.2) as measured by AGASA extended up to higher energies than was expected by the GZK theory. Eight events were observed above 10^{20} eV whereas the expected number is less than one [30].
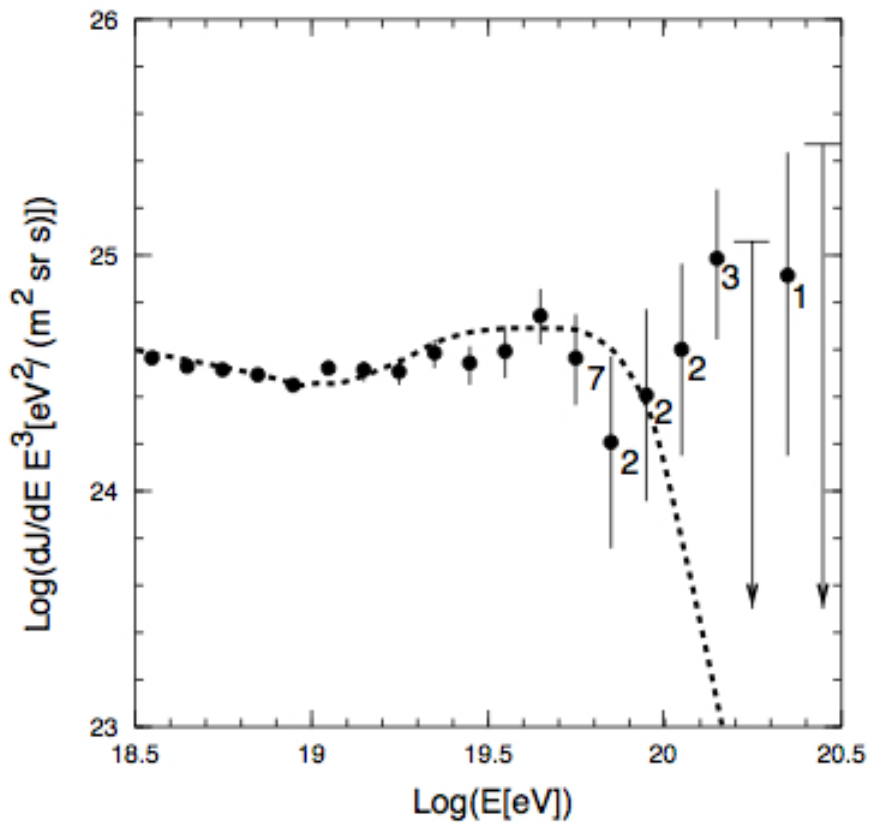

Figure 2.2.2: AGASA energy spectrum. Error bars represent the Poisson upper and lower limits at 68 % and arrows are 90 % confidence level upper limits. Numbers attached to points show the number of events in each energy bin. The dashed curve represents the spectrum expected for extragalactic sources distributed uniformly in the Universe [30].

3. While there was no large scale anisotropy observed when studying cosmic rays with energies above 10^{19} eV, a small scale anisotropy was detected. Events were concentrated in doublets or triplets in areas of less than 2.5° (Fig.2.2.3); the probability of observing such clusters by a chance coincidence is smaller than 1% [37].
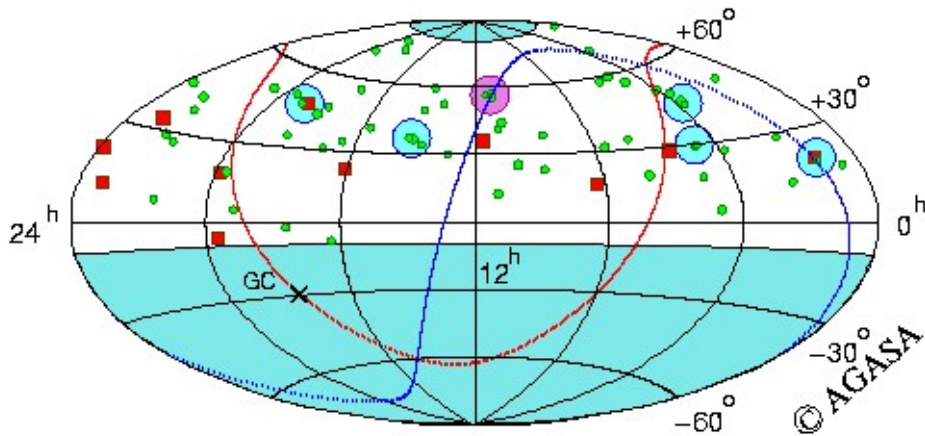
Figure 2.2.3: Arrival directions of cosmic rays with energies above 4 x 10^{19} eV. Red squares and green circles represent cosmic rays with energies above 10^{20} eV, and (4-10) x 10^{19} eV, respectively. Shaded circles indicate event clustering within 2.5° [37], [35].

4. Anisotropy was also detected in the arrival directions of particles with energies around 10^{18} eV (Fig.2.2.4). The anisotropy was interpreted as excess of showers near the directions of the Galactic centre and the Cygnus region [38].
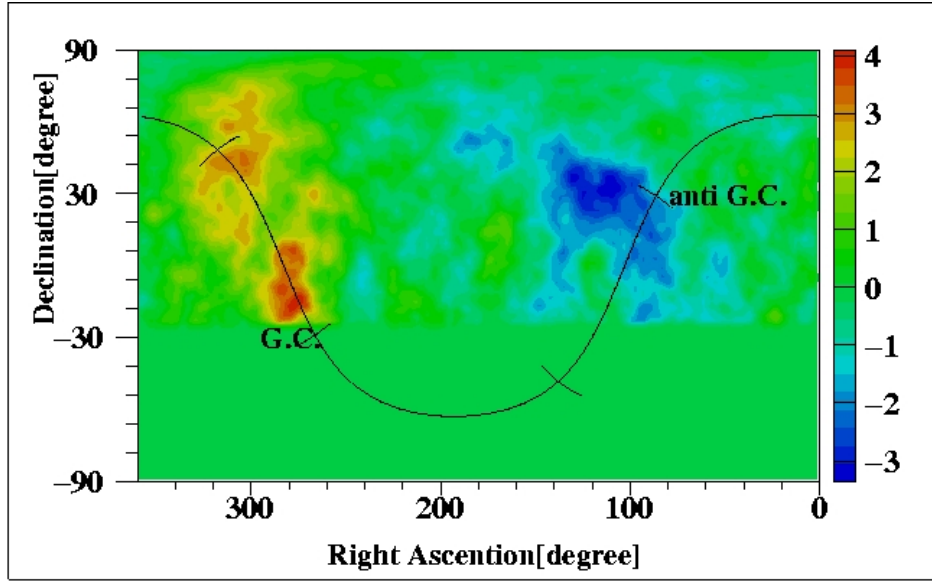
Figure 2.2.4: Map of ratio of the number of observed events to expected ones in equatorial coordinate. Solid line shows Galactic plane and G.C. marks the Galactic centre [38].

2.2.2   HiRes

The High Resolution Fly's Eye or HiRes detector was an ultra-high-energy cosmic ray observatory that operated in the western Utah desert from May 1997 until April 2006. There were two sites separated by 12.6 km. HiRes-I had one ring of 22 telescopes that took a "snapshot" of the extensive air shower generated when the incident cosmic ray interacted with the atmosphere producing fluorescent light. Meanwhile, HiRes-II had two rings of telescopes and it was able to produce movies of the cosmic ray events. Basic information can be found in [39].

 Most important results include:

1. The HiRes experiment made the first observation of the GZK cutoff at 6 x 10^{19} eV (Fig.2.2.5), with a statistical significance of 5σ [31]. This result is contradictory to the prior AGASA result.

24
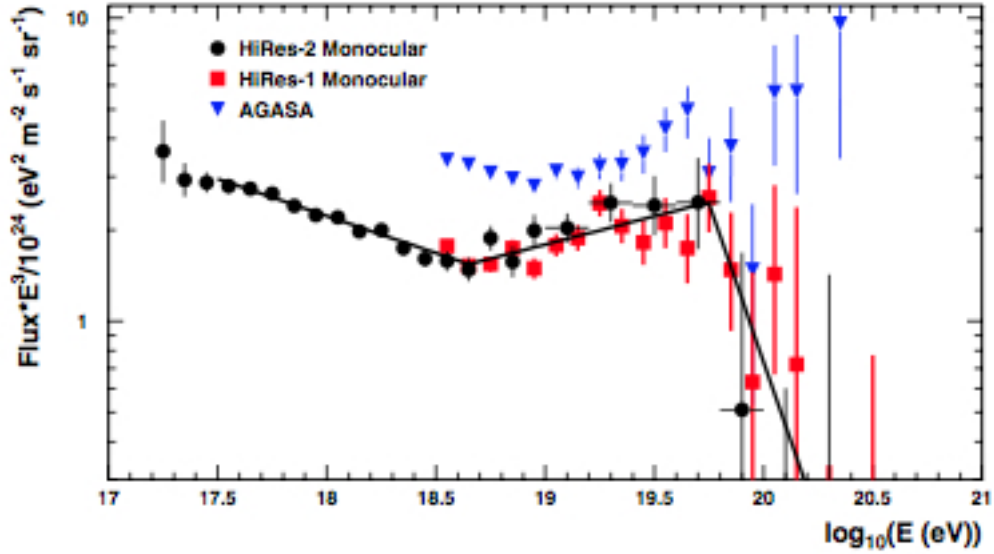
Figure 2.2.5: The cosmic-ray energy spectrum measured by the HiRes-I and HiRes-II detectors. The spectrum of the AGASA experiment is also shown [31].

2. The hypothesis of AGN (Active Galactic Nuclei) being the sources of cosmic rays was tested but there was no significant correlation discovered [40].

3. Moreover, HiRes has looked for correlation of events with the local large scale structure (LSS). No significant correlation was found at the 95% confidence level for events above 4 x 10 [19] eV [41].

2.2.3 Yakutsk EAS array

The Yakutsk Extensive Air Shower array is situated near Yakutsk, Russia and it has been operational since 1973. It studies cosmic rays of energies above 10^{15} eV. The total area covered is about 10 km^2. At present the array consists of 58 ground-based and 6 underground scintillation detector stations and 48 atmospheric Cherenkov light detectors.

Cherenkov light is emitted when a charged particle travels in a medium with a speed greater than the phase velocity of light in that medium. The particle excites the molecules of the medium and when they return to their ground state they emit photons of blue light. These photons interfere constructively and the result the detectable blue glow known as Cherenkov radiation.

In addition, there are also 5 underground muon detectors. The average distance between the particle detectors is 250 m and between the Cherenkov detectors about 500 m. Muon detectors are scattered between the other two types of detectors. Basic information can be found on the array's website [42].

Below, the most important results are summarised:

1. The GZK cutoff is present in the spectrum measured by Yakutsk [32]. Two ways of measuring the primary spectrum were used; the first one by using the light from the scintillator counters and the second one by using the Cherenkov light emitted by the relativistic electrons produced in the shower caused by the primary cosmic ray. Measuring Cherenkov light is a distinctive feature of the Yakutsk array. The resulting spectrum and a comparison with other experiments are shown in Figure 2.2.6. The "ankle" feature in the shape of spectrum below 10^{18} eV and the "knee" at about 10^{15} eV are confirmed.
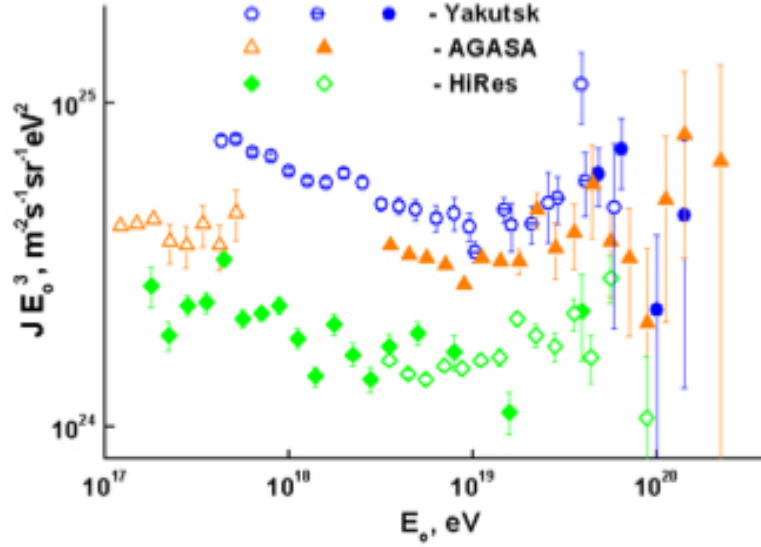
Figure 2.2.6: Differential spectrum of Ultra High Energy Cosmic Rays measured by Yakutsk and compared to AGASA and HiRes spectra [32].

2. The mass composition of primary cosmic rays has been studied by Yakutsk by examining extended air showers in the energy region 10^{15}-10^{19} eV. It has been found that from $E_0 \geq 5 \times 10^{15}$ eV, where E_0 is the energy of the primary particle, the composition gets heavier with increasing energy and after $E_0 \sim 10^{18}$ eV it becomes lighter, consisting mainly from protons and nuclei of He and C [43].

3. Cosmic rays originating from the Galactic disc have two characteristics: Galactic plane enhancement and north-south asymmetry. These characteristics can be used to detect the Galactic component of the primary cosmic ray flux. In Yakutsk an analysis of the UHECR (Ultra High Energy Cosmic Rays) - cosmic rays with energy exceeding 10^{18} eV - showed a southern excess in the energy region of 5-20 $\times$ 10^{18} eV at the significance level $\sim 3\sigma$, whereas no Galactic plane enhancement was detected. The conclusion that was

drawn was that there is indeed a non-zero Galactic component, and it was estimated to be $\sim 10\%$ of the primary flux at energy $\sim 10^{19}$ eV [44], [45].

2.2.4 Pierre Auger Observatory

As already mentioned, one of the main motives for the construction of the Pierre Auger Observatory was the contradictory nature of the results of previous experiments on the GZK cutoff. The Pierre Auger Observatory is situated in Argentina and has been functional since 2004. The Pierre Auger Collaboration includes more than 490 scientists from various countries. The observatory is designed to detect cosmic rays with energies over 10^{20} eV. It consists of 1600 water Cherenkov detectors, distributed over 3,000 km^2 with 1600 m spacing, along with 24 atmospheric fluorescence detectors to measure air showers in the atmosphere (Fig.2.2.7). Basic information can be found on the relevant website [46].

The characteristic of the Pierre Auger Observatory is that it combines both ground and fluorescence detectors thus allowing comparison and cross-checking of the data. As a result the energy calibration is improved in comparison with prior experiments.
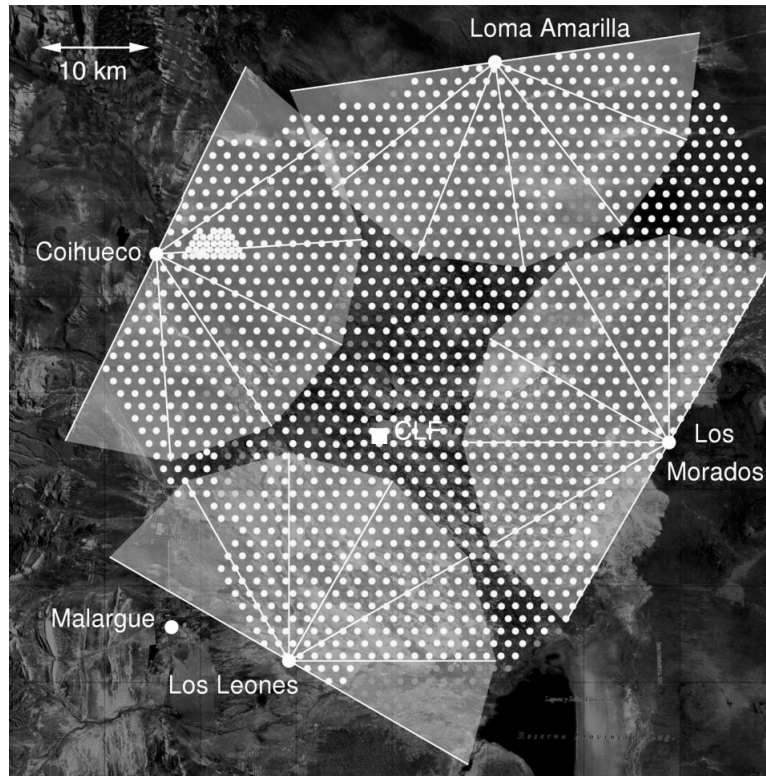
Figure 2.2.7: Status of the Pierre Auger Observatory as of March 2009. Light grey dots indicate deployed detectors, while dark grey defines empty positions. Light grey segments indicate the fields of view of 24 fluorescence telescopes [47].

A Cherenkov detector is shown in Figure 2.2.8. It is a plastic tank filled with 11,000 litres of de-ionized water. Each tank is equipped with 3 photomultipliers that detect the Cherenkov light produced when particles cross the tank. The fluorescence detector comprises 4 observation sites located atop small elevations on the perimeter of the Cherenkov detector array. Each site is equipped with 6 telescopes. A schematic of one is shown in Figure 2.2.9. Those telescopes contain mirrors covering 30° in azimuthal and zenithal angles which reflect the fluorescence light emitted by excited N_2 molecules onto an array of 22×20 photomultipliers.
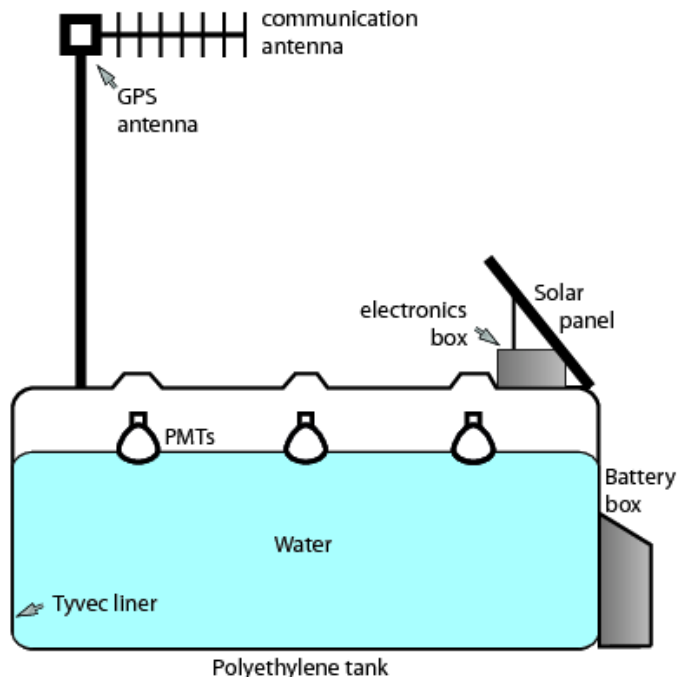
Figure 2.2.8: Schematic of a Cherenkov detector at Pierre Auger observatory [48].
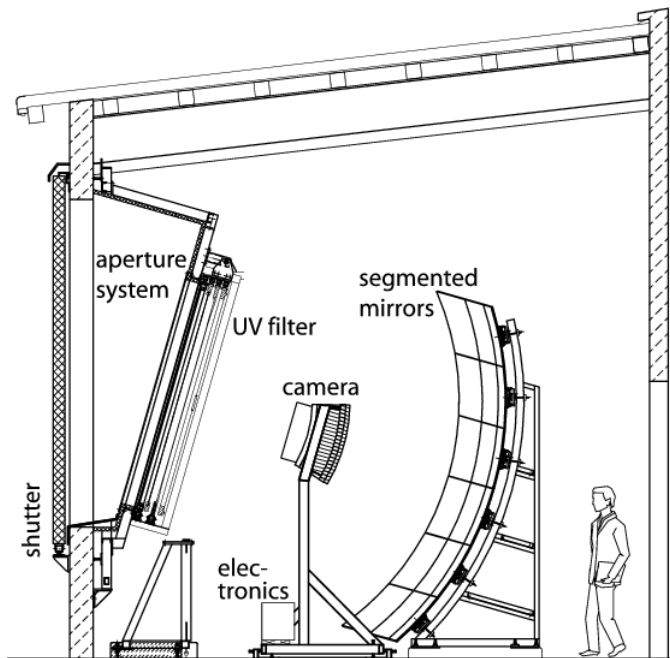
Figure 2.2.9: Schematic view of a fluorescence telescope of the Pierre Auger Observatory [47].

Below I summarise the most important results of the Pierre Auger Observatory:

1. The spectrum of cosmic rays measured by the observatory is shown in Figure 2.2.10. The most important result is the detection of the GZK cutoff [7].
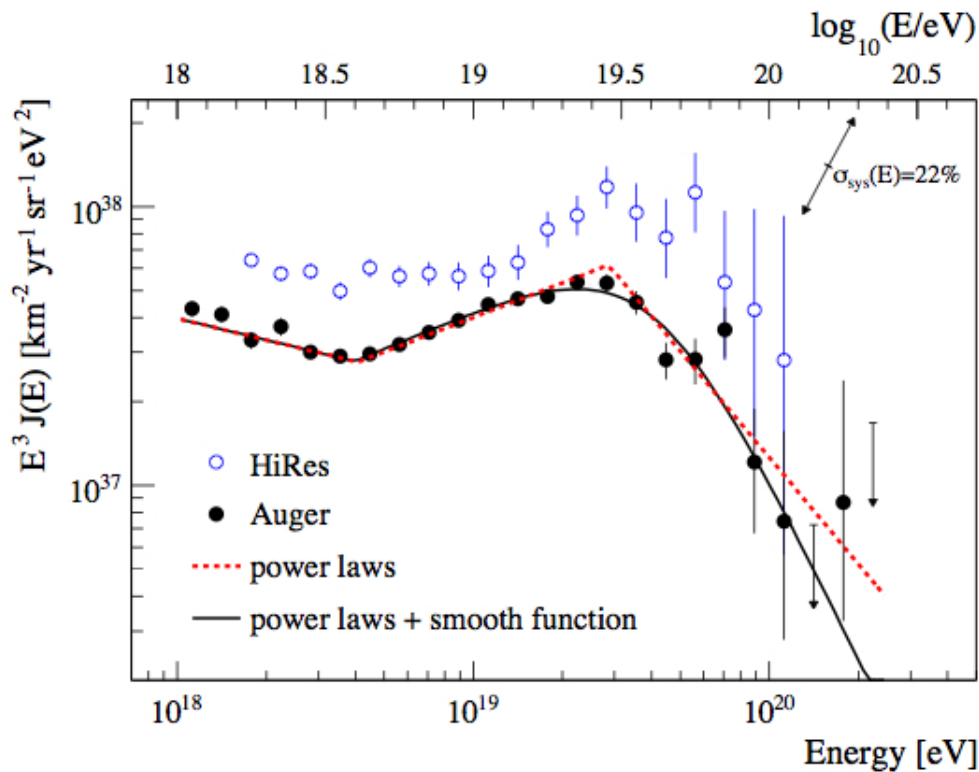
Figure 2.2.10: The energy spectrum as measured by Pierre Auger Observatory, fitted with two functions and compared to HiRes measurements [7].

2. Most of the scenarios for the composition of UHECR predict a photon component in the cosmic ray flux. The Auger Collaboration investigated the upper limits for the fraction of photons in the flux. By analysing hybrid events (events detected by both Cherenkov and fluorescent detectors) the upper limit of the photon fraction

was found to be 16% at confidence level of 95%. A second analysis was performed using data from the surface detectors only and the following upper limits for photon fractions were found: 2.0% for E>10^{19} eV, 5.1% for E>2×10^{19} eV and 31% for E>4×10^{19} eV at 95% confidence level. These results can be used to test theoretical models [49].

3. The Pierre Auger observatory is also looking for Ultra High Energy (UHE) neutrinos, specifically τ neutrinos. For this purpose almost horizontal showers are detected and analysed (zenith angle> 70°). When interacting deeply in the atmosphere at nearly horizontal incidence, neutrinos can be distinguished from regular hadronic cosmic rays by the broad time structure of their shower signals in the water-Cherenkov detectors. After almost two full years of data taking there were no candidate events found. Figure 2.2.11 shows the established limits on integrated and differential neutrino fluxes. These limits can constrain and validate models [50].
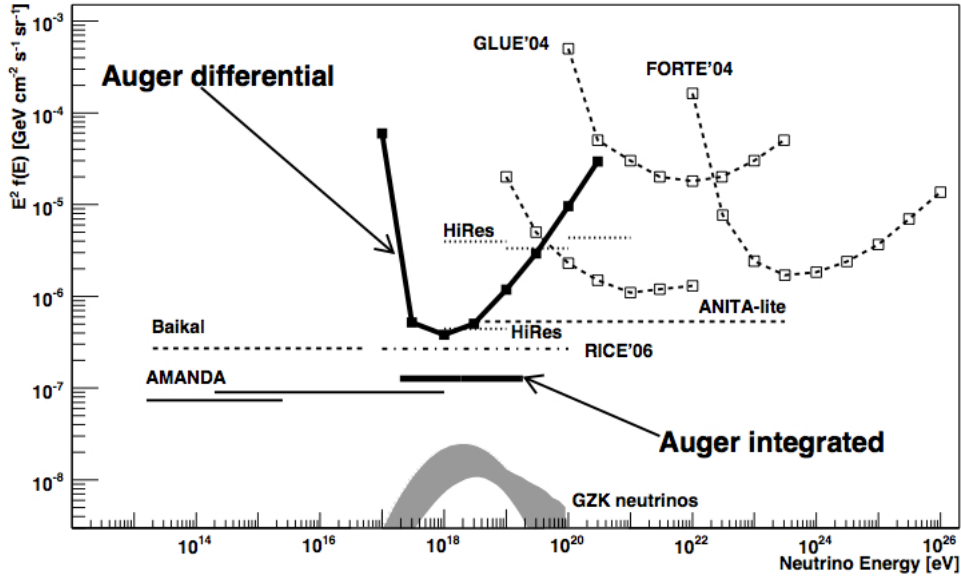
Figure 2.2.11: Limits on integrated and differential fluxes of high energy neutrinos for Auger and other experiments [50].

4. Some previous experiments (AGASA [51] and SUGAR [52]) measured an excessive flux of high energy cosmic rays $10^{18} - 10^{19}$ eV from regions close to the Galactic centre. However, Auger has not detected any anisotropies in the flux of high energy cosmic rays, other than those due to statistical fluctuations [53].

5. In a 2007 paper the Auger observatory reported on the fact that cosmic rays with energies greater than 6×10^{19} eV showed a clear anisotropic origin. A correlation between the highest energy results and Active Galactic Nuclei (AGN) was observed but this could not establish that AGN themselves are the sources because the spatial distribution of these objects coincided with other extra galactic objects [54]. In 2010 Auger reported a drop of the correlating fraction from 69% to 38%, compared with 21% expected for isotropic cos-

mic rays [55]. The latest result reports no significant deviation from isotropy [56].

2.3 Arrays based in schools

Apart from the big scientific experiments there are also ground arrays based in schools dedicated to the study of high energy cosmic rays. The idea is that students and their teachers will operate the detectors and analyse the data. There is international interest on this idea which has been put to work with successful results in various countries; for example a workshop held at CERN in October 2010 was attended by representatives of more than 20 countries. The biggest networks are HiSPARC (High School Project on Astrophysics Research with Cosmics) in the Netherlands and QuarkNet in USA. Similar smaller networks, such as the Cosmic Ray Project at King's College London, CZELTA in Czech Republic, Cosmos à l'École in France, and the Extreme Energy Events project in Italy have been constructed around the world, providing many examples of how the network can be used and what can we gain from it.

2.3.1 HiSPARC

HiSPARC is a project in Netherlands which involves secondary schools and academic institutions. The first data were collected in 2002, and the network has been expanding since then, with the UK and Denmark also involved in the project. The scientific institute Nikhef (National Institute for Subatomic Physics) in Amsterdam coordinates HiSPARC.

Besides the educational role of HiSPARC, there are also plans for

it to act as a scientific experiment investigating cosmic rays at energies between 10^{16} and $10^{19.5}$ eV. For this, the detectors are organised in clusters with typical distances between them about 50 km. Each cluster is centred around a scientific institute which coordinates and supports the local detectors.

The detectors are spread in 7 cities of the Netherlands and each city has two to seven detector stations in schools or in local universities. There is also one cluster being built around Bristol University in the UK and an operational cluster in Aarhus, Denmark. All data are upload on the HiSPARC site and graphic results are accessible by a visitor.

Figure 2.3.1: HiSPARC participating cities [57].

HiSPARC detectors consist of two plates of scintillator (BICRON BC408) about 2 cm thick with an effective area of 0.5 m^2 each, a Perspex light guide plate glued on one edge of the scintillator (Fig.2.3.3), both wrapped in highly reflecting aluminium foil and after that in light tight pond liner and a PMT (Electron Tubes 9125 SB) attached to the light guide. Everything is kept inside ski boxes in order to be protected from extreme weather conditions (Fig.2.3.4). There is also a GPS antenna (Trimble, ACUTIME 2000) installed in the vicinity of the detector. The signals from the two PMTs are read out by a coincidence unit and each trigger is combined with a GPS timestamp. This information is sent to a central service where it is compared with information from other sites and it is analysed [58].

The detectors measure coincidences and an event is triggered when a signal is read out within 1.5 μs and only if its amplitude is over 70 mV. The time window is set to make sure that the particles come from the shower and the amplitude threshold to make sure that the signal is not generated by electrons [59].
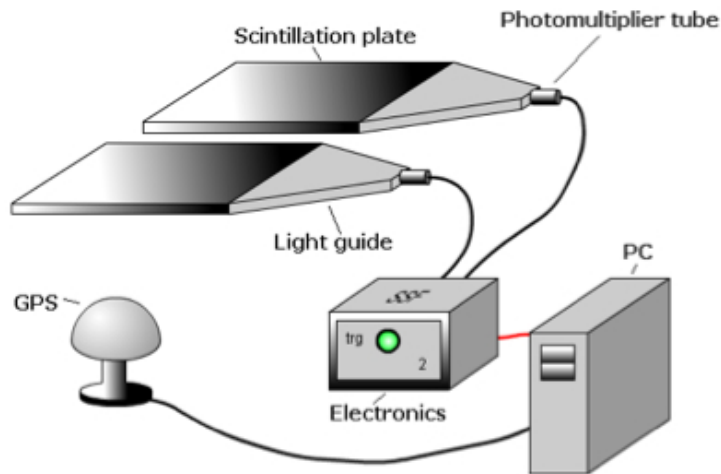
Figure 2.3.2: Outline of a HiSPARC detection system [59].

36
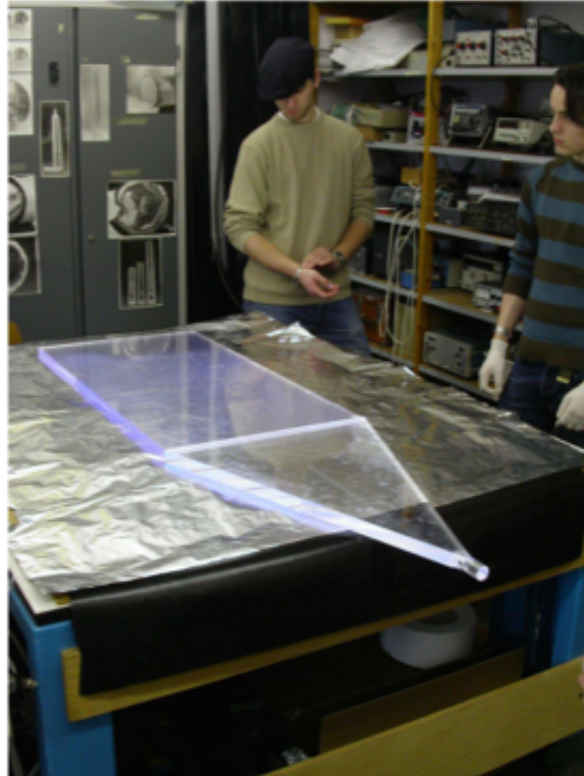
Figure 2.3.3: Scintillator plate and light-guide of a HiSPARC detector [58].

Figure 2.3.4: Two ski boxes containing HiSPARC detectors [57].

There are two ways to place the detectors: a two ski box and a four ski box configuration, the former being most suitable when the local station is part of a cluster of stations (Fig.2.3.5). A configuration with four detectors allows for a study of a shower's direction to be made.
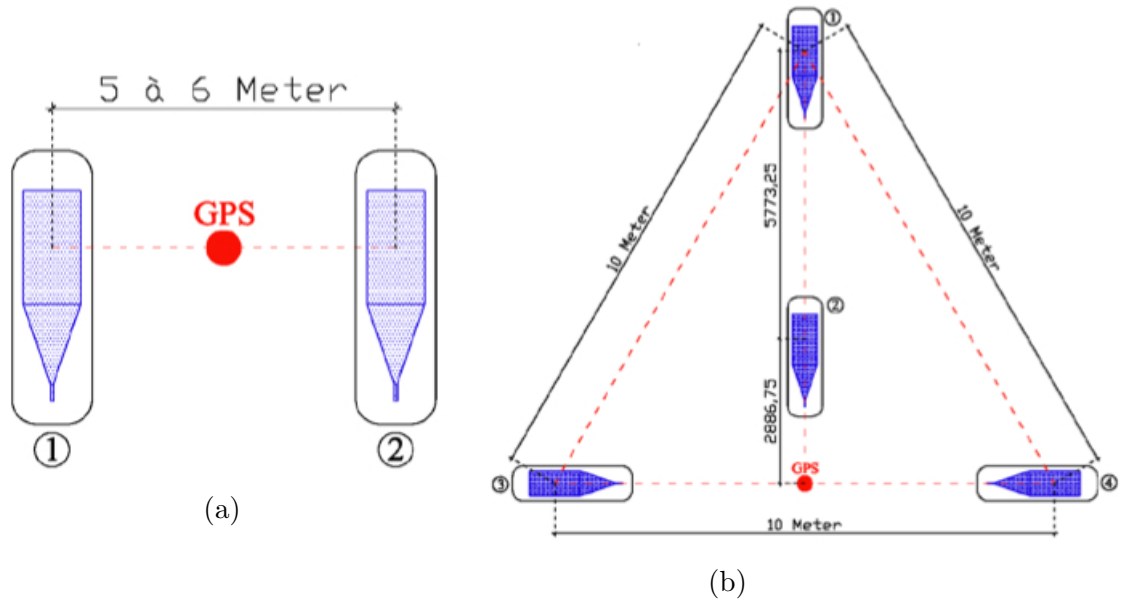
Figure 2.3.5: Two (a) and four (b) detector configurations [59].

HiSPARC has succeeded in detecting high energy events which spread more than 1 km. For example, in March 2005 an event was recorder in Nijmegen where the clustered detectors are 988, 2477 and 2780 m apart. The energy of the event was estimated to be almost 8 x 10^{19} eV while the probability of this triple coincidence was less than 3 x 10^{-4} [58].

2.3.2   QuarkNet

QuakNet is a much larger network, active in the USA. There are over 500 high schools participating and about 50 university or laboratory centres. There is a user friendly e-lab webpage [60] where any member of the

network can upload, share and analyse their data.
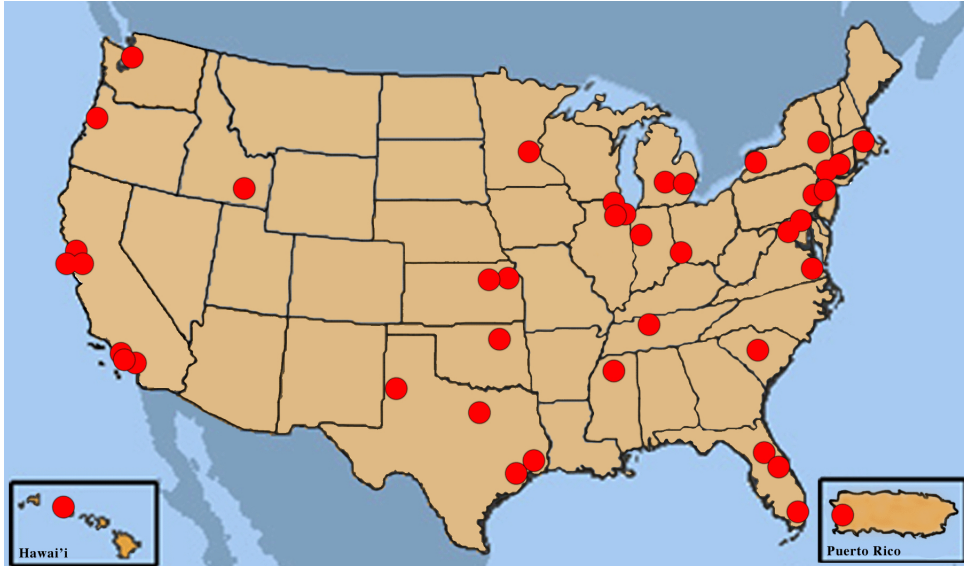
Figure 2.3.6: QuarkNet participating cities [61].

The components of the detectors used in QuarkNet are shown in Figure 2.3.7.

We used the same DAQ board and GPS unit for CORUS (information in the next section) and a detailed description can be found in chapter 3. A +5 VDC power supply is plugged into the DAQ board and it is also used to supply power to the PMTs through a power distribution unit (PDU). The PDU is a box of four potentiometers which allow one to easily change the voltage of each PMT for optimal settings. The scintillators are plastic, wrapped in foil and each one is connected to a PMT. The whole system is then wrapped in light-tight material. Everything else is similar to what we used for CORUS and information can be found in chapters 3 and 4, including user commands, data display and possible experiments.
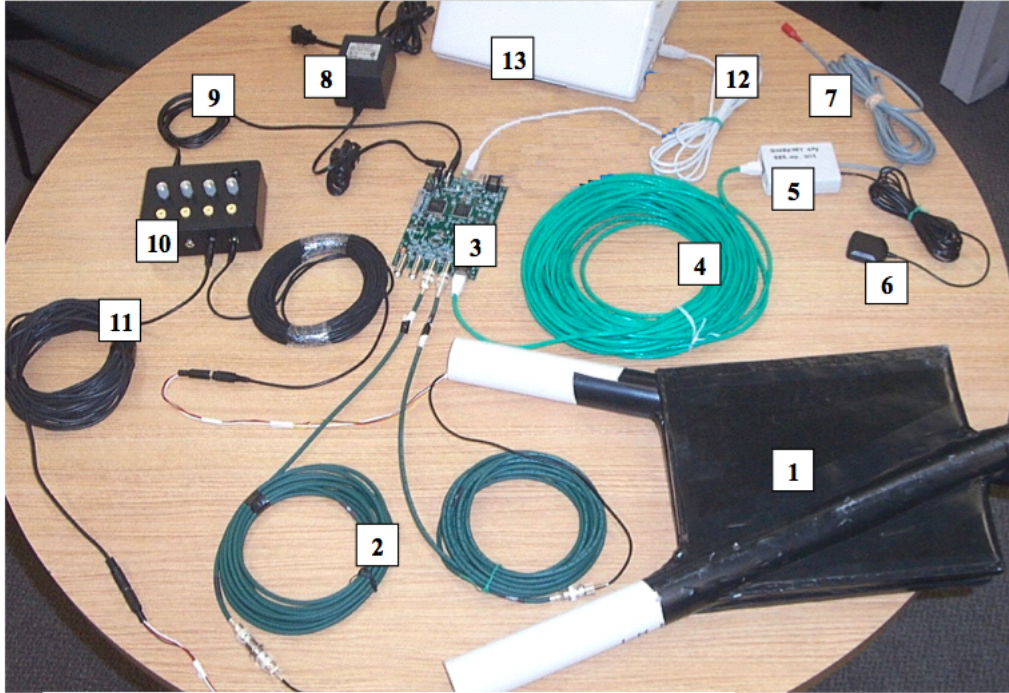
Figure 2.3.7: Components of a QuarkNet detector: 1) Counters: scintillators, PMTs and PVC housing, 2) BNC signal extension cables, 3) QuarkNet DAQ data acquisition board, 4) CAT-5 network table, 5) GPS module, 6) GPS antenna, 7) Temperature sensor, 8) 5 VDC power supply, 9) PDU power cable, 10) Power distribution unit, PDU, 11) Power extension cables for PMTs, 12) USB cable, 13) PC [62].

2.3.3 The CORUS project

The CORUS (Cosmic Rays in Uk Schools) projects aims at bringing "real" science in schools around the UK. The main objective of the project is to start a national array of cosmic ray detectors in schools, building on a smaller scale pilot project around the UK. The pedagogical aim of the project is to motivate students aged 16-19 to get more interested in science by offering them the opportunity and means to design and execute real experiments. In the UK it seems necessary to motivate students towards science as is shown by the small number of

students 16-19 years old who are taking courses in physical sciences [63]. The deficit of graduates to train as physics teachers is also a fact [63], [64] and although the numbers have increased recently [65], there is still the need to maintain the rise. The CORUS project offers a perfect opportunity to do that. The hands-on approach can be proven very beneficial for students, and they can be inspired to get more involved in science. It has been observed that students who choose a physics degree have often been motivated by "cutting-edge" physics such as particle physics and astrophysics [66]. The physics of cosmic rays falls exactly between these two disciplines. In addition, the advantages of using muon detectors as a means to motivate students are:

- The underlying technology is well-established and not difficult to implement.

- The costs of such detectors are not prohibitive.

- A set of cosmic rays detectors provides teachers with a tool to explain aspects of particle physics, cosmology, astrophysics and astronomy whilst also allowing the students to develop key skills such as teamwork, application of number and problem solving.

The students, after having been introduced to cosmic rays and having familiarised themselves with the equipment, can perform various experiments. The types of experiments that can be performed include calibration and performance studies, muon lifetime experiments, shower studies, or flux studies as a function of one or many variables, e.g., time of day, solar activity, east/west asymmetry, angle from vertical, barometric pressure, etc. During the project, students will:

41

- Get in touch with particle physics concepts and learn about muons particularly.

- Practise designing the optimal experiment for their scientific purpose.

- Learn to handle raw data from real experiments.

- Learn to interpret results from their data and give them a physical context.

- Practice expressing their results in writing.

- Gain experience on experimental measurements and handling equipment.

- Gain computing skills.

- Learn to work in teams and divide the workload.

- Compare results and methods with other teams and gain knowledge from that.
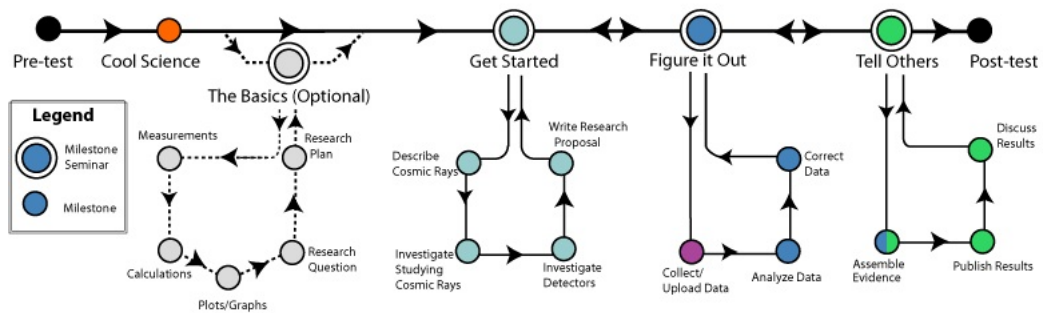
- Practise oral and poster presentation.

Figure 2.3.8: Schematic showing the workflow of a QuarkNet projec [60].

CORUS objectives include the following: a) to deploy a number of detectors (initially about 30) in schools in the UK, b) to develop a web site to disseminate information about the project, c) to develop support material for teachers and students, d) to work with European partners on issues such as common formats to permit exchange of data, e) to hold regular teachers' conferences and occasional teacher and pupil-led workshops to facilitate dissemination and future planning for the project.

The detectors are expected to be used as A level educational material. However, they will also be accessible by younger children, in particular those in Y11 and the intention of CORUS is to develop support material for GCSE level as well as AS/A2 to be able to be part of the project. It is estimated that more than 150 students each year are in A level and in Y11 about to make subject choices (all of whom are required to do some science) per school. For 30 detector units, this gives us more than 4500 students per year to participate in the project and take advantage of the multiple gains mentioned above.

2.4 Conclusions

In this chapter I presented the most important ground arrays dedicated to cosmic rays and their recent results. I also presented the motivation of the CORUS project, emphasising on the importance and role of such educational tools in UK schools. The two most successful existing networks (HiSPARC and QuarkNet) were described in order to make clear that such projects are viable and well received by the educational community in other countries.

An extensive description of a CORUS detector is following in chapter 3. I also compare the HiSPARC and QuarkNet systems and explain what led to the decision to build a detection system similar to QuarkNet.

Chapter 3

Components of a CORUS detector

3.1 Introduction

In this chapter I will discuss the equipment that was used to build a prototype CORUS detector. I first compare the two candidate electronics systems, HiSPARC and QuarkNet, and explain why the latter was chosen. A detailed presentation of the prototype detector and of each of its components follows.

3.2 System comparison (HiSPARC - QuarkNet electronics)

Initially, two systems were considered to be used for the CORUS project: the QuarkNet system and the HiSPARC system. QuarkNet is a network of detectors operating in over 500 schools in USA and HiSPARC is a very

large network of school detectors mainly in Netherlands, both described in chapter 2.

The two main differences between the two systems are: a) the way the detectors are run and the data are uploaded and analysed and b) the kind of data that are recorded. In HiSPARC, the detectors are monitored remotely and there is no need for daily on-site intervention. The data is transferred and analysed automatically on a central database. In QuarkNet on the other hand, each school is responsible for keeping the detectors running, recording the data via the relevant software, uploading and analysing it. The procedure is explained in detail in chapter 4. As a result the QuarkNet system allows for more flexibility, as students can choose a subject to experiment on (muon flux, muon lifetime, shower detection, etc) and they can alter the working modes of the detectors (singles count, 2, 3, 4-fold coincidence, threshold setting, etc) whereas the HiSPARC system measures coincidence events and it is oriented towards detecting showers both on a small (one school) and a large scale (cluster of schools).

Along with being more flexible, another major benefit of the QuarkNet system is the cost: US$150 per channel for QuarkNet, compared to €750 per channel for HiSPARC. It is important to keep the costs for each school to a minimum and since the electronics are the most expensive part of the detector, the QuarkNet system has a clear advantage. Overall, the total cost per school (3 QuarkNet detectors and installation) is about £3000.

3.3 Components of the detector

The basic design of a muon detector consists of the following elements: a) a scintillating material (solid or liquid) i.e. a material that will absorb incoming particles and re-emit the energy as light, b) a way to transport the light (fibres or light guide), c) light-detecting equipment, d) a read-out system to read and analyse the data.

For the CORUS prototype detector we assembled a system which consists of three wooden boxes with each box holding nine scintillator tiles lined with optical fibres and a photomultiplier tube collecting the light from the fibres. A coupling system is attached to the PMT in order to connect it to the fibres so that minimum light is lost. A DAQ board is used to gather the PMT output and input it to a PC which is used to control the DAQ board using commands, read the information from the board and analyse the data on the network's website. The wooden skeleton and the light-proofing of the first box was made at the University of Leeds. The mechanical workshop of Durham University constructed the other two boxes and I light-proofed them. The coupling cylinder was produced by the mechanical workshop as well, under my instructions. The scintillators were manufactured at IHEP (Institute for High Energy Physics) in Moscow, Russia. The prototype interface board that accompanies the PMTs was made at the University of Bristol by Dr David Cussans and the two duplicates at the electronics workshop of Durham University. All tests that were performed and described below were contacted by myself, as well as the experiments of chapter 4. Next I describe each element individually and explain the motivation behind

the choices we made.

3.3.1 Detector Box

The most important consideration for the box that holds the scintillator tiles, the fibres and the photomultiplier with the coupling system is to be light-tight so that we have the minimum photon contamination of our data. For our example detector we used a box constructed at the University of Leeds shown in Figure 3.3.1 and two other similar boxes created at Durham University.

Figure 3.3.1: Example box design, created at the University of Leeds

The box itself is made out of wood and it measures about 90 cm x 50 cm. It holds the scintillator tiles wrapped in foil, the optical fibres and the PMT with the coupling system. Foil keeps incoming light out and reflects photons back to the scintillator to be detected. The box is also lined with pond liner and the volume that remains is filled with a piece of foam, both keeping the light out. Furthermore, the foam keeps

the equipment in its place in case of moving the box.

3.3.2 Scintillator

Inside each detector box there are 9 plastic scintillator tiles measuring 15 cm x 15 cm x 0.5 cm, produced at IHEP (Institute for High Energy Physics) in Moscow, Russia. They absorb incoming particles and reemit the absorbed energy as light, specifically blue and ultraviolet photons. The advantage of plastic scintillators is that they can be shaped easily and that they have fairly high light output and a relatively quick signal. The scintillator is transparent to the light produced in it so the photons are not absorbed again. Other advantages of the Russian scintillators are that they are cheap, each tile has 3 grooves where optic fibres are laid to collect the light, and they can be produced in bulk if needed.

Figure 3.3.2: Scintillator tiles, produced in Russia. The optic fibres inside their grooves are also visible.

3.3.3 Optical fibres

Wavelength-shifting optical fibres are laid along the grooves of the scintillator tiles. The fibres (BCF-92 by Saint Gobain) absorb the ultraviolet and blue photons and emit green light (emission peak at 494 nm). The spectrum is shown in Figure 3.3.3. Because of the change in wavelength, the critical angle is reduced and the green light can escape only at the end of the fibre and not though its internal walls.
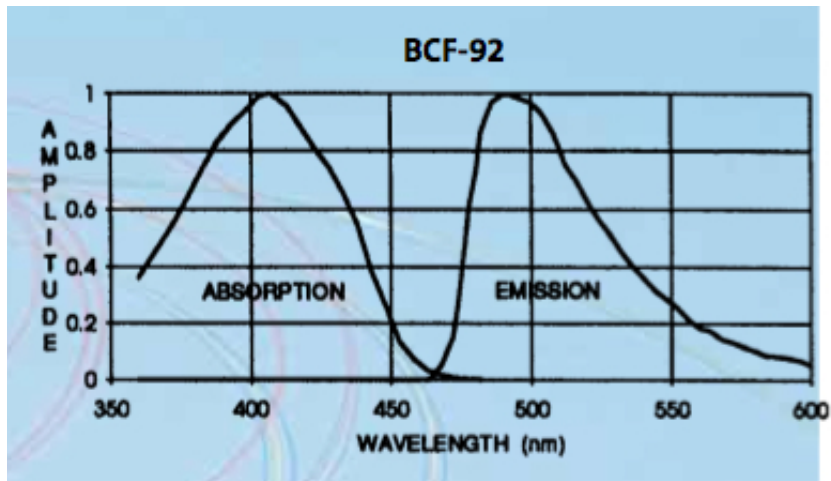
Figure 3.3.3: Absorption and emission spectra of BCF-92 optical fibres by Saint Gobain [67].

One end of the fibre is sealed with Tippex so that the light is reflected back. The other end is coupled to a photomultiplier tube using a system described in the next section. We chose to use optical fibres instead of a light guide (i.e. a piece of Perspex attached to the scintillator and to the PMT) because of the time saving in manufacture and their physical flexibility, plus the Russian scintillators are already grooved.

I tested whether if we put double fibres in each groove the average height of the pulses observed on an oscilloscope is bigger. This hypothesis

was based on the idea that the photons produced by a passing muon would be measured from two fibres simultaneously and the amount of energy deposited on the photomultiplier photocathode would be double, thus giving a bigger pulse to the oscilloscope. No significant difference was observed in the average height of the measured pulses i.e. the average height remained (9 ± 2) mV. Therefore I used a single fibre in each groove of the scintillator tiles.
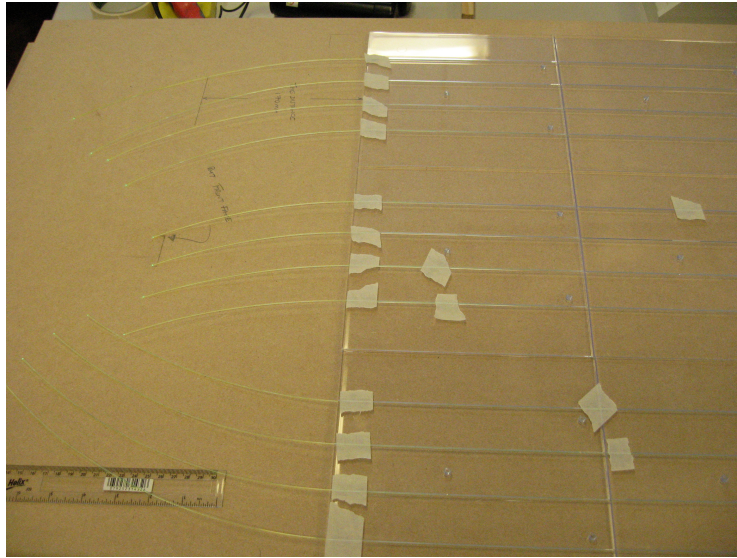
Figure 3.3.4: Wavelength-shifting optical fibres placed in the grooves of the scintillator tiles. The fibres are BCF-92 by saint Gobain and they emit green light.

3.3.4 Coupling system

The need to couple the fibres to the photomultiplier became clear when we arranged the fibres in a bunch and put them in the photomultiplier opening so that their end is as close as possible to the photocathode, without using the perspex cylinder. This way we got almost no pulses from the system due to the air between the fibres and the cathode.

For this purpose I produced a Perspex cylinder exactly matching the diameter of the photomultiplier tube. Perspex is a common glass substitute. It transmits up to 92% of the visible light coming from the fibres and has the advantages of being more light weight and shatter-resistant than glass. On one end of the cylinder there are 24 holes where the optical fibres are inserted and their diameter matches the diameter of the fibres. We initially drilled 24 holes so we could use double fibres in each groove of the scintillator. The reason for that was to test whether the use of double fibres in the grooves of the scintillator would make any significant difference in the response of the system as described in the previous section. As the result was negative, only 12 holes of the 24 were used in the final design. The holes extend about 1.5 cm into the cylinder in order to allow a secure connection of the fibres and at the same time ensure the cylinder would not shatter.

I tried different arrangements of the holes on the cylinder (Fig.3.3.5). Initially we produced a Perspex cylinder with the holes arranged in a straight line across the diameter (a). This was then compared with a circular arrangement, (b). The average pulse height with the circular arrangement was (9±2) mV and with the linear arrangement was (4±2) mV. As expected, the circular arrangement is an improvement, due to the reduced sensitivity of the PMT photocathode towards the edges.

(a) First
arrangement (not
used)

(b) The second and final
arrangement

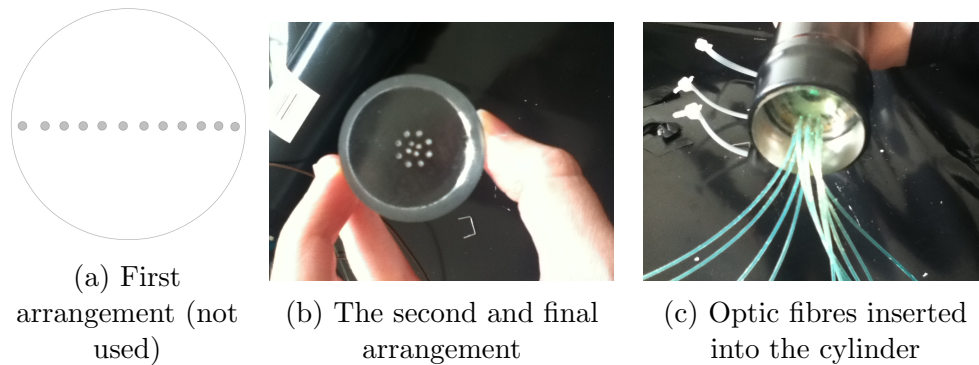(c) Optic fibres inserted
into the cylinder

Figure 3.3.5: The coupling cylinder and the different arrangement of
the fibre hole that were tested.

Prior to insertion, it is necessary that the fibres are dipped into optical couplant to achieve a better optical connection at the bottom of the hole. I used an index matching gel manufactured by Minilink which reduces the difference in the index of refraction at the interface of the two surfaces (optical fibre and bottom of the hole). Optical couplant is also used at the end of the cylinder which is attached to the photomultiplier. Without it the read out pulses are very limited in number, almost 1 or 2 pulses per minute compared to over 10 pulses per minute that are measured with the use of the gel.

3.3.5 Photomultiplier tube and interface board

Photomultipliers work by the photoelectric effect. A photon exiting the coupling cylinder strikes the photocathode and if its energy is greater than the work function of the photocathode material, then an electron is liberated. The electron enters the electron multiplier, which consists of a number of dynodes. There the number of electrons is multiplied by the process of secondary emission. As the electron approaches the

first dynode, it is accelerated by the electric field so its energy increases. When it strikes the first dynode, more low energy electrons are emitted and these electrons in turn are accelerated as they approach the second dynode. The process is repeated several times, thus an avalanche of electrons is created. When the electrons reach the anode, a measurable current has been created which can be shown as a pulse on an oscilloscope.

The photomultipliers used are type R580-12 by Hamamatsu (Fig.3.3.7). They were used at the ZEUS calorimeter at HERA (Hardon-Electron Ring Accelerator) which is in DESY, the German research centre. The diameter is 38 mm, it has 10 dynodes and it is sensitive to wavelengths from 300 nm to 650 nm with maximum response at 420 nm.
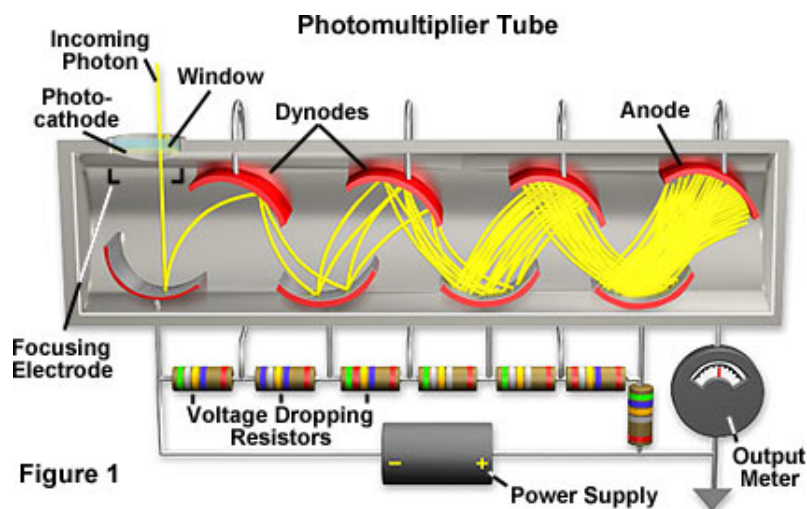

Figure 3.3.6: Diagram of the work principles of a photomultiplier. Light is gathered in the photocathode where electrons are liberated. An avalanche of electrons is created by striking consecutive dynodes and the current is measured at the anode [68].
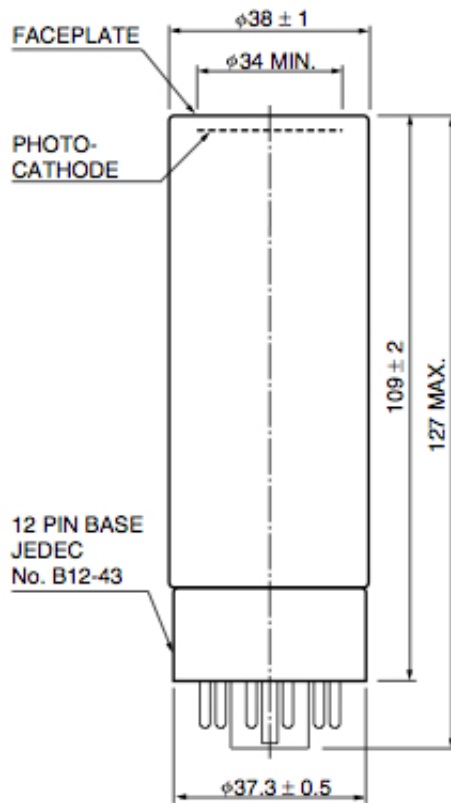
Figure 3.3.7: Diagram of the Hamamatsu R580-12 PMT [68]. All values are in mm.

The electron multiplier needs a high voltage source to operate. The high voltage base that is used for this purpose uses a resonant converter and a Cockcroft-Walton (CW) chain. The Cockcroft-Walton chain or multiplier is an electric circuit, made up by a series of capacitors and diodes, which generates a high DC voltage from a low voltage AC or pulsing DC input. Figure 3.3.8 shows a simple two-stage CW chain. The operating voltage of the PMT is 1300 V and the distribution of high voltages from anode to the first dynode is according to the ratio 3: 2: 2: 2: 1: ... :1: 2 [69].

Figure 3.3.8: A two-stage Cockcroft-Walton chain electric circuit [70].

With this system very little energy is wasted in heat and the necessary supply voltage is only 24 V. Thus there is no need for a high voltage box which costs more and is not safe for use by school children. It 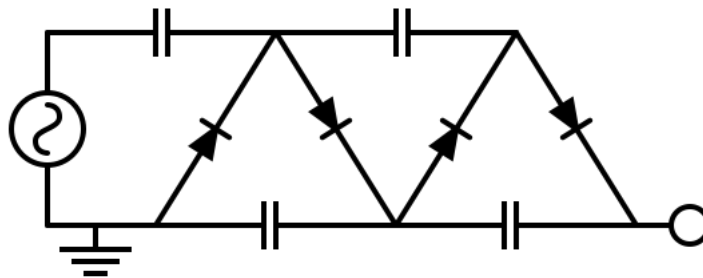also protects the PMT from short circuits. The Cockroft-Walton chain and the safety it provides is one reason why we chose these specific PMTs. Another reason is that they are readily available in large numbers.

The voltage is supplied through an interface board created at the University of Bristol. The output pulses also pass through the board which carries a pulse amplifier. The idea is to maintain the fast rise of the pulse but to increase the fall time so that it is visible on a low-bandwidth oscilloscope that schools are likely to have. It also boosts the signal amplitude and the gain is controllable through a switch. During the course of this study one of the main objectives was to test whether the QuarkNet electronics worked well with the elongated pulses (chapter 4). Schematics of the electronics on the board are shown in Figure 3.3.9.
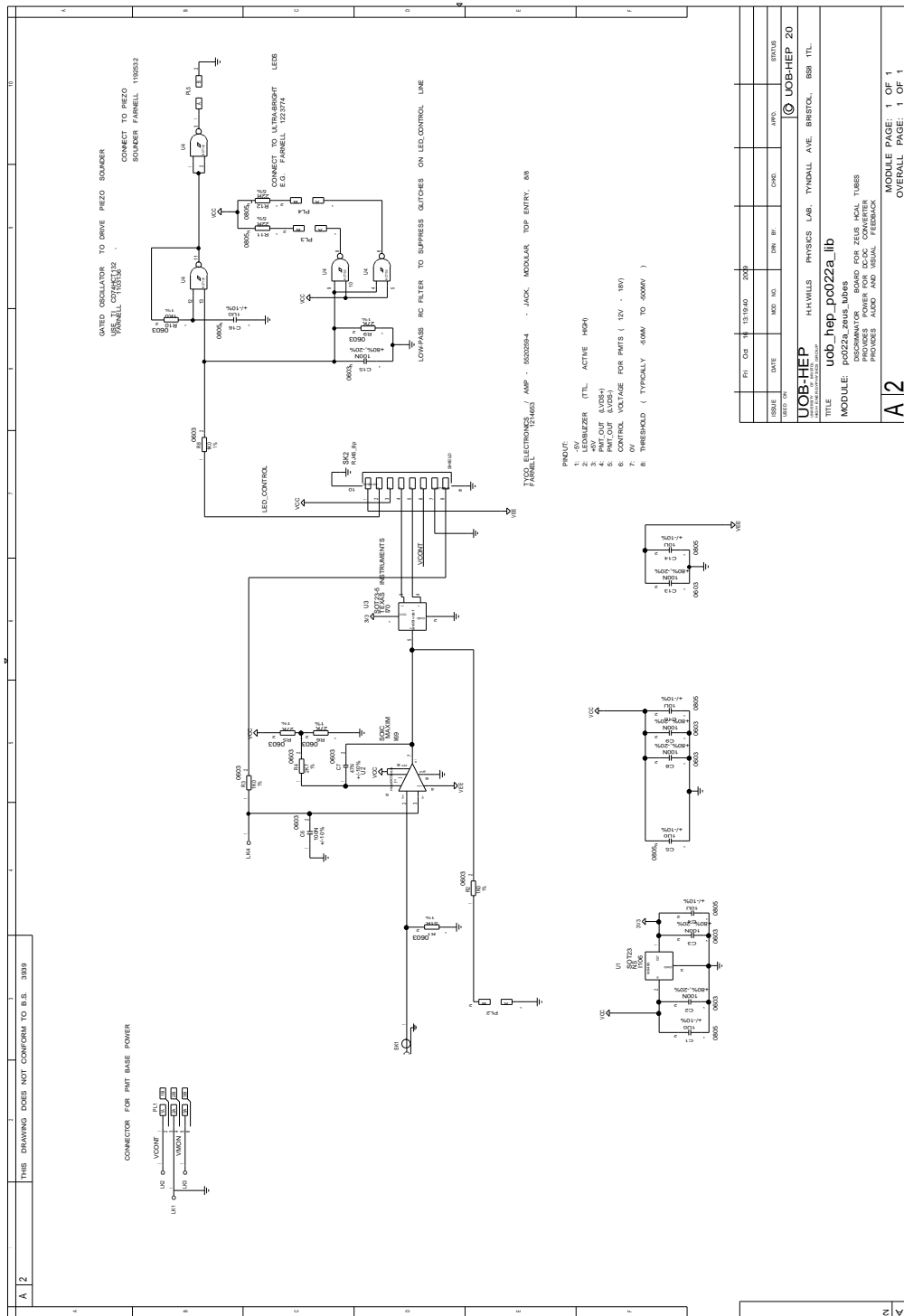
Figure 3.3.9: Circuit diagram of the PMT support board (Dr David
Cussans, private communication)

3.3.6 QuarkNet DAQ board

Figure 3.3.10 shows the QuarkNet DAQ board. This board is the "brain" of the whole detection system providing the link between the scintillation counters and the PC. All information relating to board information is taken from [62] and [71].
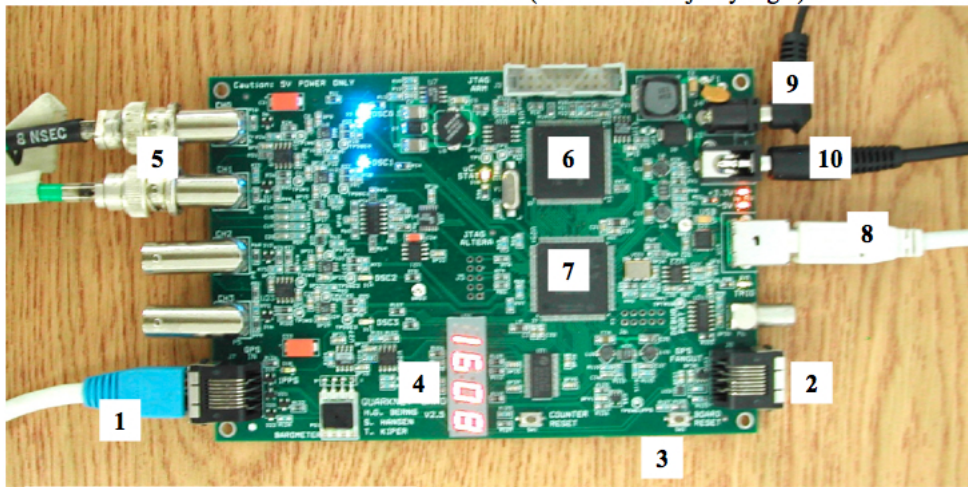
Figure 3.3.10: The QuarkNet DAQ board. 1: GPS input, 2: GPS fanout to another DAQ board, 3: Board reset button, 4: LED display, 5: Inputs for 4 counters, 6: Complex Programmable Logic Device (CPLD), 7: Time-to-digital converter, 8: USB board (output to PC), 9: 5 VDC input, 10: 5 VDC output to power distribution unit [62].

The DAQ (Data Acquisition) board can take signals from up to four PMTs, analyse them and send the output data to a PC. The output data include information about the number of channels that had above-threshold signals, their relative arrival times, leading, trailing edge times for each pulse recorded within the coincidence time window and GPS data. An external GPS receiver module gives the UTC time of each trigger to a resolution of 10 ns. This allows schools to correlate their data. Furthermore, we can measure the time difference between pulses

58

on different channels in the same site down to less than a nanosecond (resolution 1.25 ns). This enables schools to demonstrate the existence of air showers and estimate the direction of the incoming cosmic ray.

Figure 3.3.11: Workflow of the QuarkNet DAQ board [71].

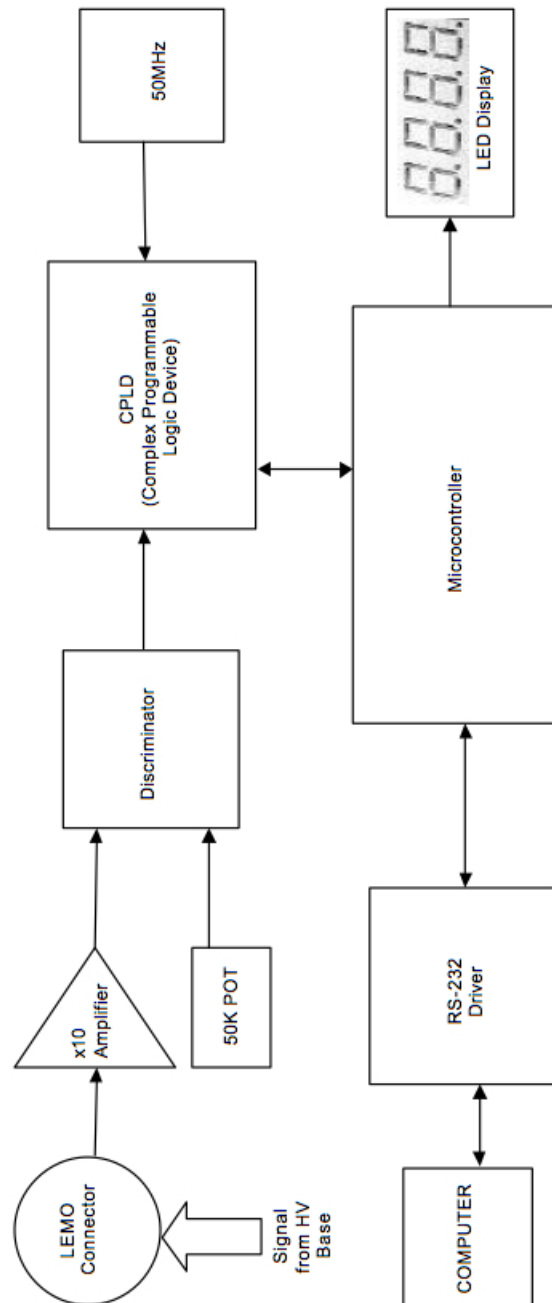A diagram of the workflow of the board is shown in Figure 3.3.11. The signal cables are attached to the board using BNC connectors. PMT signals are amplified x 10 in order to be big enough for the discriminator to read and to reduce the effect of the noise. The potentiometer sets the threshold voltage for the discriminator.

The discriminator compares the signal to the threshold and outputs a 1 or 0 signal, indicating whether the level has been met. The discriminator output pulse is fed into a TDC (Time-To-Digital-Converter). The TDC data give leading and trailing edge time for each channel and we can calculate the ToT (Time over Threshold) which gives us a good estimate of the pulse area, thus the energy of the pulse.

It is important to set the right threshold level in the voltage comparators of the discriminators, so that we neither miss any events, nor measure background noise. In order to do that we make a plot of the event frequency versus the threshold voltage. The threshold value after which the frequency decreases much more slowly is the optimum voltage.

The coincidence logic of the DAQ board is operated by the Complex Programmable Logic Device (CPLD) and works as follows: whenever a channel goes above threshold a time window is opened. If any other channel goes above threshold during this time window, all event data are latched and outputted for the overlap time interval when both are active (this example is for a 2-fold trigger criterion). Leading and trailing edge times are reported for any active channels and not just the two that launched the trigger, with empty data entries for the channels that remained inactive during the trigger window. The time of the trigger window can be set by the user. Each channel can also be individually

enabled or disabled by the user. The coincidence level can be set from one to four, one meaning counting only single hits. Examples of how the coincidence logic works can be found in chapter 4.

There is a 50 MHz crystal oscillator clock on the board which sets the frequency for the CPLD at 20 ns/cycle. The oscillator acts also as a clock for the microcontroller.

The configuration parameters for the CPLD can be set through the microcontroller which also acts as the main buffer. It checks all data and displays it to the user terminal. The microcontroller also keeps individual scalers for each channel as well as a total trigger scaler which can be displayed on the user terminal upon request by command.

The RS-232 driver acts as an interpreter between the controlling PC and the microcontroller.

The LED display on the board can be set to show single or counts coincidence counts so the user can perform very basic measurements and also control the functionality of the board.

There are two temperature sensors, one measuring the temperature of the CPU and the other the ambient temperature. In addition, a barometric pressure sensor is built into the board, which can be used to monitor the atmospheric pressure while measuring the muon flux.

There are five counters on the board numbered 0-4. Counters 0-3 record the single counts for each channel while counter 4 records the trigger count for the coincidence logic we have set. Each of the counters can be individually enabled or disabled.

The board requires a stable +5 VDC power supply, with 800 mA or greater output current.

The GPS module should be put outdoors or, if inside, near a window where in will be able to see at least half the sky. It will quickly lock its position onto four or more satellites. The GPS unit gives the exact time as well as exact coordinates (latitude and longitude) of the location of the detector. It also outputs a logic pulse at the beginning of each UTC second, called the 1PPS (1 Pulse Per Second) signal.

The data stream displayed on the PC is in ASCII format. each line contains 16 words as shown in Figure 3.3.12. A single event can produce several lines of data. Words 1-9 are in hexadecimal format. Below is a description of each of the words.

```
80EE0049 80 01 00 01 38 01 3C 01 7EB7491F 202133.242 080803 A 04 2 -0389
80EE004A 24 3D 25 01 00 01 00 01 7EB7491F 202133.242 080803 A 04 2 -0389
80EE004B 21 01 00 23 00 01 00 01 7EB7491F 202133.242 080803 A 04 2 -0389
80EE004C 01 2A 00 01 00 01 00 01 7EB7491F 202133.242 080803 A 04 2 -0389
80EE004D 00 01 00 01 00 39 32 2F 81331170 202133.242 080803 A 04 2 +0610
```

Figure 3.3.12: Sample event as displayed on a PC, producing several lines of data. Each line has 16 words [62].

Word 1: A 32-bit trigger count of the 25 MHz CPLD clock mounted on the DAQ board. When all digits are zero the board is still in initialisation phase and the data are not to be used.

Word 2: Rising edge at input 0. It is also the trigger tag. The format used is as follows: bits 0-4 are the count of the rising edge, bit 5 is the channel edge tag (1=valid rising edge, 0= no rising edge), bit 6 is not used, always 0, bit 7 is the trigger tag (1= new trigger, start of a new event, 0=follow-up data of a trigger event).

Word 3: Falling edge at input 0. The format used is similar to the rising edge format except bit 7 which is not used and it is always 0.

62

Word 4: Rising edge at input 1. Same format as in word 2 except bit 7 is always 0.

Word 5: Falling edge at input 1. Same format as in word 3.

Word 6: Rising edge at input 2. Same format as in word 4.

Word 7: Falling edge at input 2. Same format as in word 3.

Word 8: Rising edge at input 3. Same format as in word 4.

Word 9: Falling edge at input 3. Same format as in word 3.

Word 10: A 32-bit CPLD count of the most recent time mark from the GPS receiver.

Word 11: UTC time of most recent GPS receiver data update. The format is HHMMSS.mmm where HH=hour (00...23), MM=minute (00...59), SS=second (00...59), mmm=millisecond (000...999).

Word 12: UTC date of the most recent GPS receiver data update. The format is ddmmyy where dd=day of the month (01...31), mm=month (01...12), yy=year (00...99).

Word 13: A GPS valid/invald flag where A=valid and V=invalid.

Word 14: The number of GPS satellites visible. This is a decimal number between 00...12.

Word 15: This hexadecimal word is a DAQ status flag.

Word 16: The time delay in milliseconds between the 1PPS pulse and the GPS data interrupt.

A schematic of the board is shown in Figure 3.3.13.
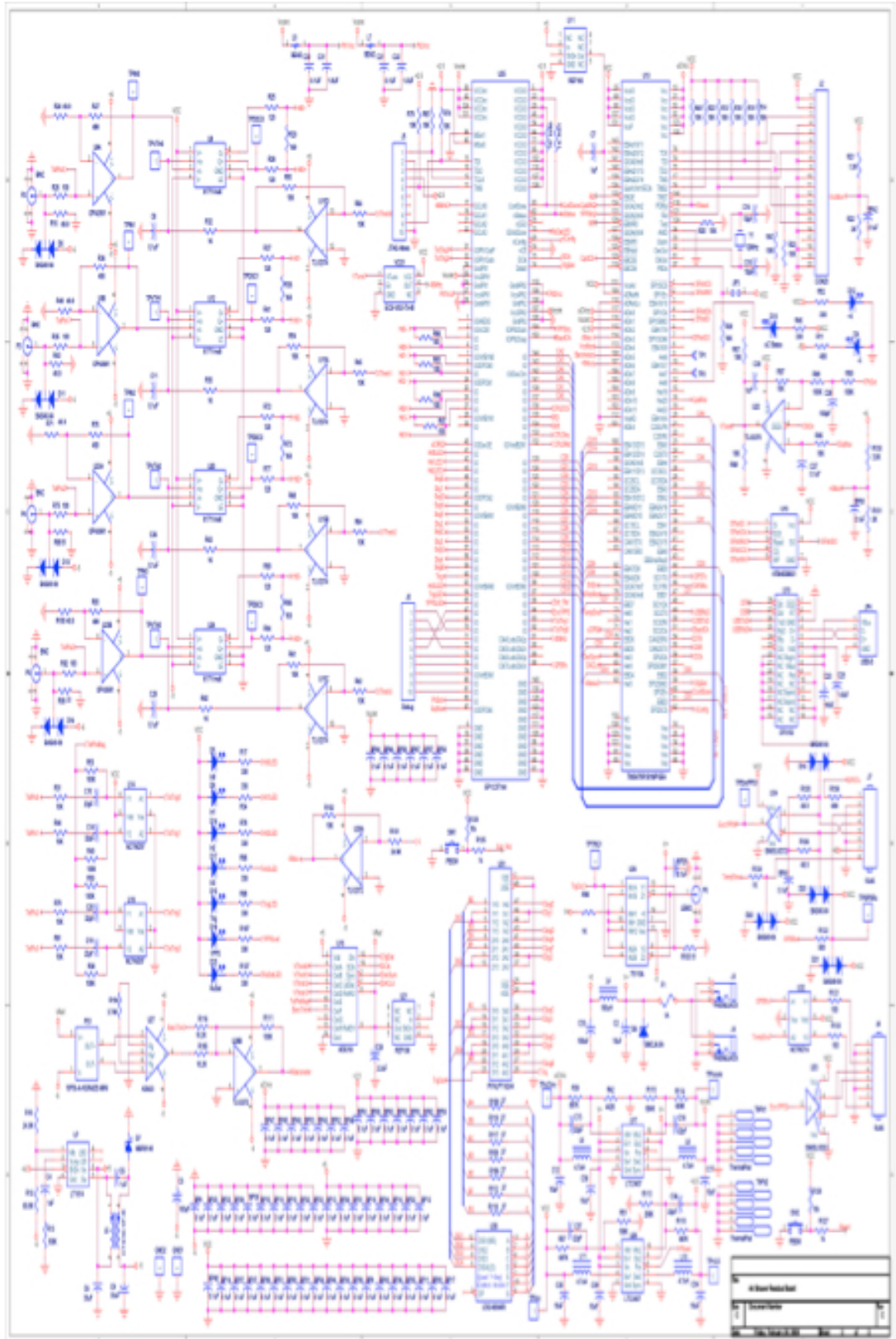
Figure 3.3.13: Schematics of the QuarkNet DAQ board.

3.4 Conclusions

This chapter gives all the information necessary to understand the way a prototype CORUS detector is designed. Besides the functionality, the flexibility and the quality of the components used, emphasis is given on the costs of each one so schools can afford to participate in the project.

In the next chapter I will discuss the experiments students and their teachers can perform with such a detector.

Chapter 4

School Experiments

4.1 Introduction

In the previous chapter I explained the reasons why we chose to set up our detectors with the QuarkNet electronics. Here I will further describe how I optimised the QuarkNet board to make it compatible with our detection system (PMTs and small interface boards). Next, I describe experiments students can perform which yield real scientific results such as measuring the flux of muons and estimating the lifetime of a muon, and I discuss the possibility of detecting cosmic ray showers with our detectors.

4.2 Gate width and TMC delay

There are two quantities that can be adjusted by the user and they are important in experiments that require coincidence measurements. The first is the gate width and the second the TMC (Time Memory Cell, name

of the specific time-to-digital converter used in the DAQ board) delay.
Each pulse is associated with these two quantities described below.

The TMC is the time by which each pulse is delayed. The gate width
refers to the time window after a pulse that a trigger may happen. For
example the trigger for a 2-fold coincidence is on when time windows are
active in any two channels at the same time. If the delayed pulses are
within the trigger window then they are read out and recorded and if
not they are ignored. Below I describe two examples to make clear what
these quantities mean, where I use the usual QuarkNet values i.e. the
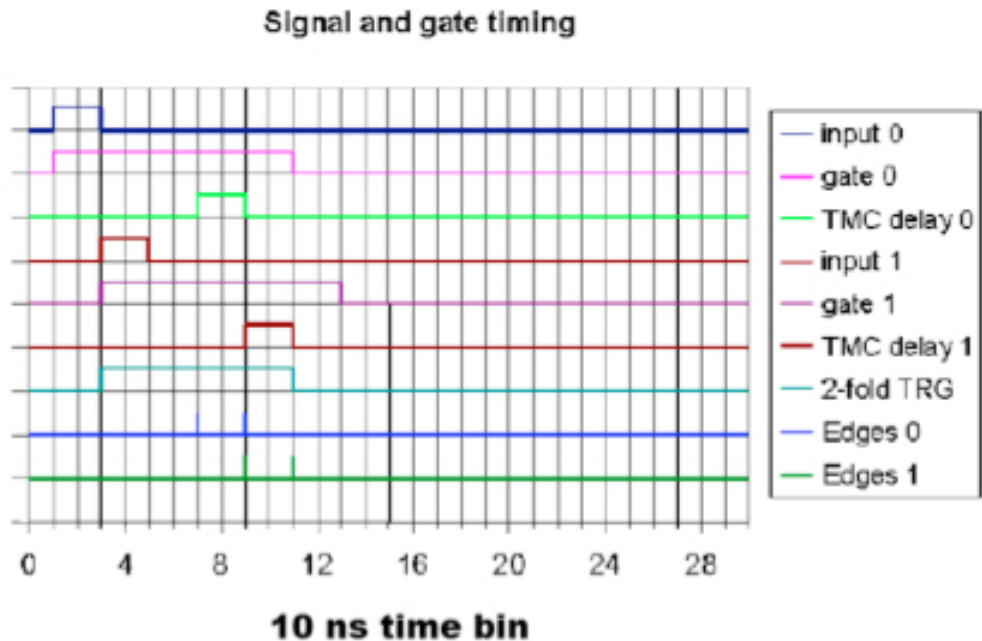gate width is 100 ns and the TMC delay is 60 ns and the coincidence
level is two.

Figure 4.2.1: Example 1 of a trigger event [62].

In the example of Figure 4.2.1 a pulse of 20 ns occurs in channel 0
(input 0). This opens a "window" of 100 ns (gate 0) while the pulse

67

itself is delayed by 60 ns (TMC delay 0). The former quantity is the gate width and the latter the TMC delay. A second pulse appears in channel 1 (input 1) 20 ns later and as a result a window of 100 ns is opened (gate 1) and the pulse is delayed by 60 ns (TMC delay 1). The trigger (2-fold TRG) is on while both windows (gate 0 and 1) are active, in this case from 30 ns to 110 ns i.e. it lasts 80 ns. Only the rising and falling edges of the delayed pulses that are inside this time frame are read out and all other information is lost. In this example both rising and falling edges of the pulses are recorded (edges 0, edges 1).
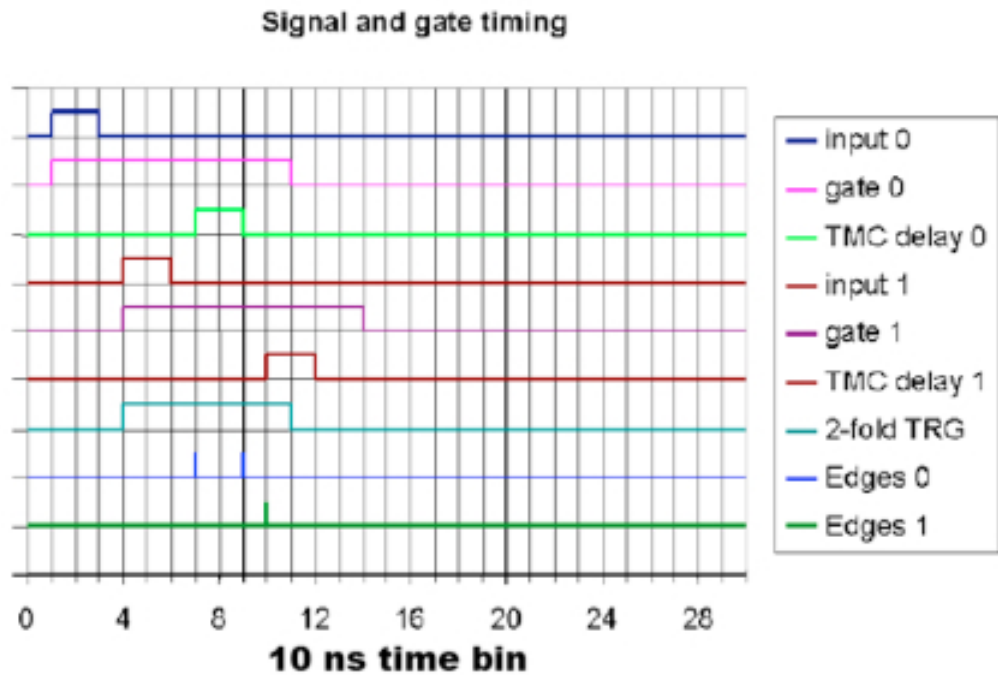

Figure 4.2.2: Example 2 of a trigger event [62].

In our second example (Fig.4.2.2), a pulse of 20 ns occurs in channel 0 (input 0). A time window of 100 ns is opened (gate 0) and the pulse is delayed by 60 ns (TMC delay 0). The second pulse (input 1) arrives 30 ns later, a window of 100 ns is opened (gate 1) and the pulse is delayed by

60 ns (TMC delay 1). The time during which the trigger is on this time is from 40 ns to 110 ns i.e. 70 ns (2-fold TRG). The rising and falling edge of the first pulse are both inside this interval and they are recorded (edges 0) as is the rising edge of the second pulse (edges 1). However, the falling edge of the second pulse lies outside the window therefore it is not recorded.

All of the above concern experiments that require coincidences between detectors, at least on a 2-fold level. In most of the experiments described in this chapter I measured single counts unless otherwise specified. As mentioned in chapter 3 the interface boards that are connected to the PMTs elongate the pulses to 200 ns, so that they are readable by any low frequency oscilloscope. If the TMC delay is X s then the gate width should be at least (200+X) s for both rising and falling edges to be read. I used the pre-set TMC value of 40 ns so my gate width should be at least 240 ns.

For the muon lifetime experiment we want to measure the electron pulses after the muon has decayed (more details for this experiment can be found in section 4.6). The average muon lifetime is 2.2 μs, hence I set the gate width to 10 μs and this value was used throughout the course of all the experiments.

4.3   Use of software

In order to operate the board through a PC, Hyperterminal or ZTerm are needed. Here I give the instructions on how to operate either one.

Hyperterminal: Upon opening Hyperterminal, a window named "Con-

nect to" will open. The port where the DAQ card is connected on the laptop is selected. On the next window, the rate is set to 115200 Bits per Second and the Row Control to Xon/Xoff. Afterwards Capture Text→Start Capture is selected from the Transfer menu and the program is started. Everything will be written to the file specified by the user. To stop data collection Capture file→Stop is selected.

ZTerm: If using ZTerm the port should be auto-detected. If not, the shift button should be held down when opening ZTerm. This will open a window where the serial port connection can be selected. Again, the Data Rate is changed to 115200 and the Flow Control to Xon/Xoff. To start data selection Start Capture is selected from the File menu, the file is specified and the program started. To stop, Hang up is selected from the Dial menu.

4.4   Calibration and performance studies

Students can perform experiments to study the response of the system. These experiments include plateauing the detectors, selecting the threshold and calibrating the barometer. These experiments are very useful when executed at the beginning of a student study because they help students familiarise themselves with the equipment and the techniques used.

All the commands that are used for the experiments of this study are already structured and used by the QuarkNet system. A complete catalogue can be found at the end of this chapter.

4.4.1 Threshold selection

The first thing to do before performing any further experiments with the detector is to determine the threshold i.e. how big a pulse should be in order to be counted. This study was conducted with one detector box, which was equipped with a prototype interface board from Bristol.

Execution

The Bristol board operates at 24 V according to its manufacturer. Based on that I kept the operating voltage constant and while gradually changing the threshold voltage through the command TL 1 d, where d is the value of the voltage, I measured the counts during a minute three times and the average was used. The results are shown in Table 4.1.

threshold voltage (mV)	N (counts/min)	uncertainty (counts/min)	relevant uncertainty (%)
10	1254	35	3
20	634	25	4
40	234	15	7
50	140	12	8
70	85	9	11
80	69	8	12
90	50	7	14
100	48	7	14
120	45	7	14
200	24	5	20

Table 4.1: Threshold measurements

Analysis

The data are plotted in Figure 4.4.1. The correct threshold value is the point at which the counts become almost constant. The reason for this is that the noise spectrum is much steeper than the signal spectrum and

71

this is why we get a "turn" in the plot. This way we can be sure that we are measuring particles with minimum noise contamination. For the first detector box I determined the threshold value to be at 90 mV (Fig.4.4.1).
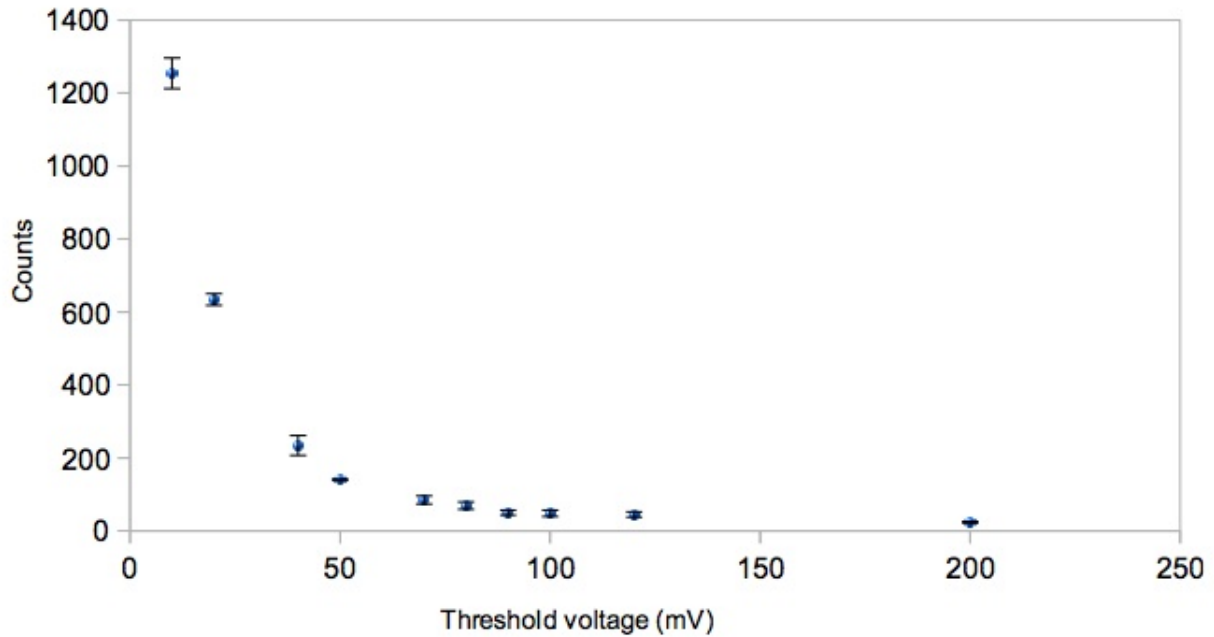

Figure 4.4.1: Threshold determination curve. The threshold is set at 90 mV.

This threshold was also set for the other two detector boxes since they have exactly the same design and the same material was used for every component. The choice was confirmed by checking the minimum height of pulses corresponding to particles on an oscilloscope for all three detector boxes and finding it the same (about 9 mV). The DAQ board amplifies the pulses x10, so we expect the threshold to be in the region of 90 mV.

4.4.2 Plateauing the detector

The next step is to plateau the detector i.e. to find the optimum operating voltage for the PMTs. In order to do that we need to produce a plot of the counts per minute as a function of the voltage and find the plateau created. Each of the three PMTs in each of the boxes used a different interface board. The first board was made in Bristol and the other two copies in Durham. The Bristol board came with the manufacturer instruction to set the operating voltage at 24 V for use with the specific PMTs and so there was no need for plateauing. However, the Durham boards required this process to be undertaken.

The fact that the operating voltage of the Bristol board was known was the reason why I chose to first find the threshold for this board, apply this to the other two boards and then proceed to plateau the detectors.

Execution

A measurement of the counts in one minute was taken for different values of the operating voltage which was changed manually. Each measurement was repeated three times and the average was used for the plot. The results are in Tables 4.2 and 4.3.

operating voltage (V)	N (counts/min)	uncertainty (counts/min)	relevant uncertainty (%)
21	18	8	44
22	14	4	29
23	16	4	25
24	16	4	25
25	33	6	18
26	28	5	18
27	30	5	17
28	30	5	17
29	37	6	16

Table 4.2: Plateauing detector 2.

| operating voltage (V)	N (counts/min)	uncertainty (counts/min)	relevant uncertainty (%)
16	10	3	30
17	28	5	18
18	34	6	18
19	71	8	11
20	152	12	8

Table 4.3: Plateauing detector 3.

Analysis

The plots for the two detectors are shown in Figure 4.4.2. The plot for detector 2 shows two plateaus, one that ends at 24 V and another that ends at 28 V. The plateau we are looking for is the latter because from then on the number of counts increases indefinitely. The first plateau is probably due to the electronics of the interface board, which were not very sensitive to the change in the voltage. We can also understand this from the fact that in detector 2 the counts go from (14±4) counts/minute to (37±6) counts/minute while the voltage has changed 7 V, whereas in detector 3 they go from (10±3) counts/minute to (152±12) counts/minute for a voltage change of only 4 V. For detector 3 the plateau is quite clear

around 18 V.
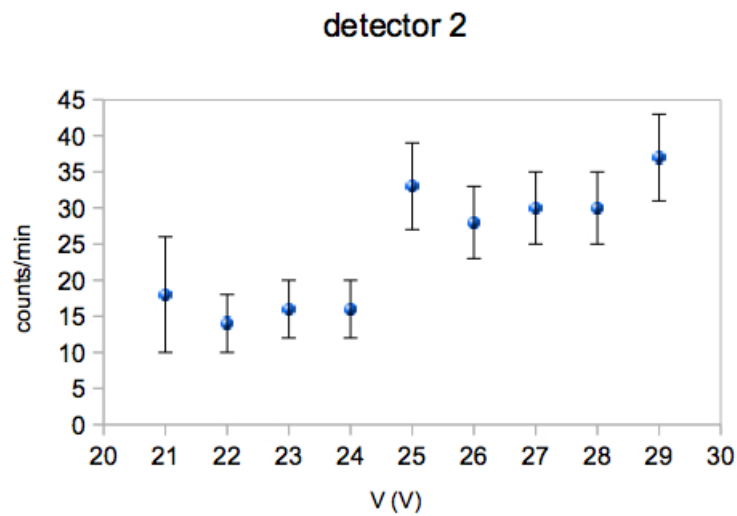
detector 2
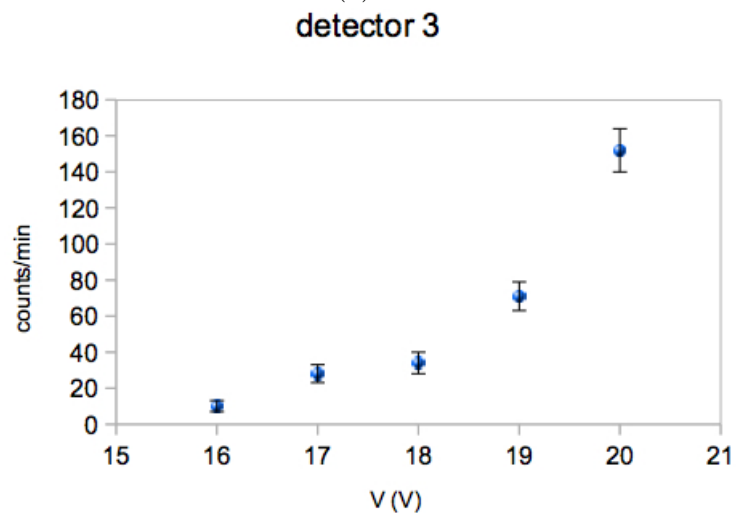
detector 3

Figure 4.4.2: Plots of the counts per minute as a function of the board operating voltage for the two detector boxes created in Durham. We can see the plateau, especially in the second plot. The operating voltage is chosen to be 28 V for detector 2 and 18 V for detector 3.

There is another way to plateau the detectors which perhaps produces a clearer graph for the students to determine the optimal voltage. Two detector boxes are stacked together and measurements of the rate

of coincidence between them are taken as a function of the operating voltage of the bottom detector. There should be a clear plateau after the optimal operating voltage because this means that all the muons that were measured from the top detector and reached the bottom have been measured (Fig.4.4.3). Afterwards the same procedure is done for the remaining detectors. This experiment was not conducted by me because of initial problems getting the detectors to measure coincidences.
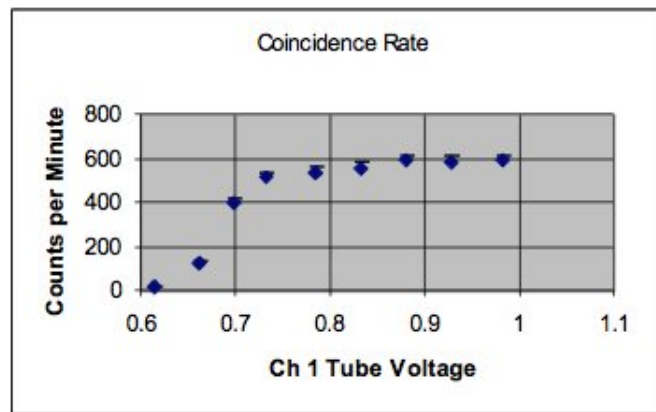

Figure 4.4.3: Example of a graph of the coincidence rate of two stacked detectors, showing the plateau and the optimal operating voltage at about 0.7 V [62]. The graph serves only illustrative purposes, as different detector components were used.

4.4.3   Performance study

The objective of a performance study is to determine the quality of the data i.e. the level of noise contamination. Noise signals are produced by other ionising particles passing through the detector, by light leaking in the boxes or by random signals in the PMT itself. In order to do this, we make a histogram of the number of the events as a function of ToT (time over threshold). ToT is the time the pulse has been over the

threshold that has been set. This is a measure of the energy deposited in the scintillator in a way, because the greater the energy, the bigger the pulse and the ToT.

The data can be uploaded onto the cosmic ray e-lab [60] and analysed there. The e-lab is an online environment useful for both teachers and students. Teachers can register their school as part of the QuarkNet network and find tools for implementing the project in the classroom and students can find problem ideas and questions about cosmic rays, upload their data, analyse both their own and other schools' data and upload their posters. The geometry of each school detector must be uploaded on the site and then students can use the different analysis tools for each experiment to process the data. The use of the e-lab is very convenient because students don't have to develop their own software, both raw data and results can be easily shared, and results from different schools are all in the same format for immediate comparison.

In the performance study the ideal is to produce a Gaussian curve with the peak corresponding to the actual muons that pass through the detector (Fig.4.4.4). We expect muons to be of a certain energy more or less, so the pulse height and also the ToT will be about the same for all muons. In reality the shape of the histogram is a skewed Gaussian with additional peaks in smaller ToT, corresponding to noise signals.
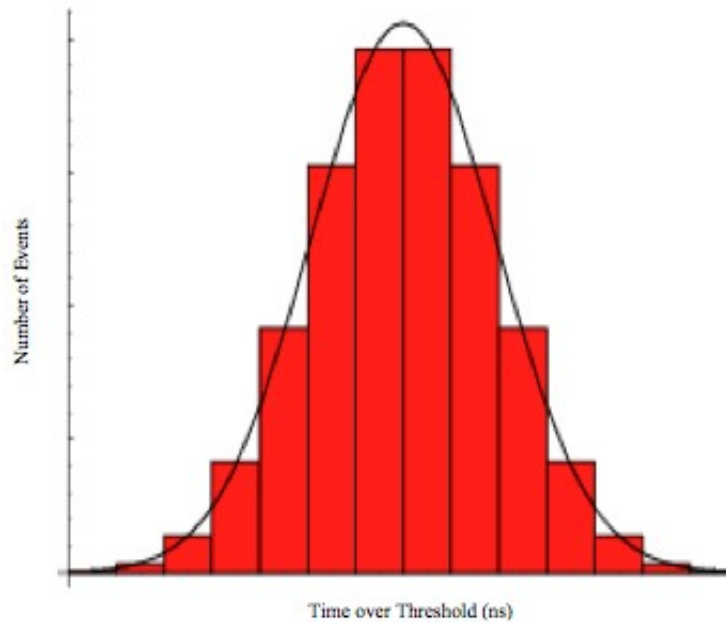
Figure 4.4.4: The Gaussian distribution expected from an "ideal" system performance [62].

Execution

For this experiment we stack our detectors one above the other and we type the following commands into Hyperterminal:

WC 02 e8 and WC 03 03 (Sets the gate width to 10 μs).

TL 4 090 (Sets the threshold to 90 mV).

V1 (Prints enabled channels, coincidence level, gate width and voltage threshold).

V2 (Sets up pressure and temperature registers).

DG (Prints date and time, status of GPS (it should be A=valid), number of satellites used, latitude, longitude and altitude).

TL (Prints the set threshold).

WC 00 0F (Sets the coincidence to 0, thus measuring only singles in each

channel).

ST 2 5 (Prints a status line every 5 minutes. Without this command the file which will be produced will not be able to be read by the online software of e-lab).

RB (Resets the counters to zero).

If everything is set correctly we press CE to start the flow of data.

Pulses were recorded from each detector for $\sim$24 hours. The data flow was stopped by typing CD.

Analysis

The analysis is done with the online software of the cosmic ray e-lab, after uploading the data. We must also upload information about the detectors, as the geometry of their arrangement (stacked or spread), the location information from the GPS (longitude, latitude, altitude) and the surface area of the detector.

The online analysis gives the option to choose the number of bins of the histogram. This is important because the shape of the histogram can change significantly. I chose the bin width to be 5 ns. Using smaller or bigger bin widths results in periodic artefacts in the plots indicating a mismatch between the bin size and our time resolution (Fig.4.4.5). My analysis produced the following graphs (Fig.4.4.5 and 4.4.6).
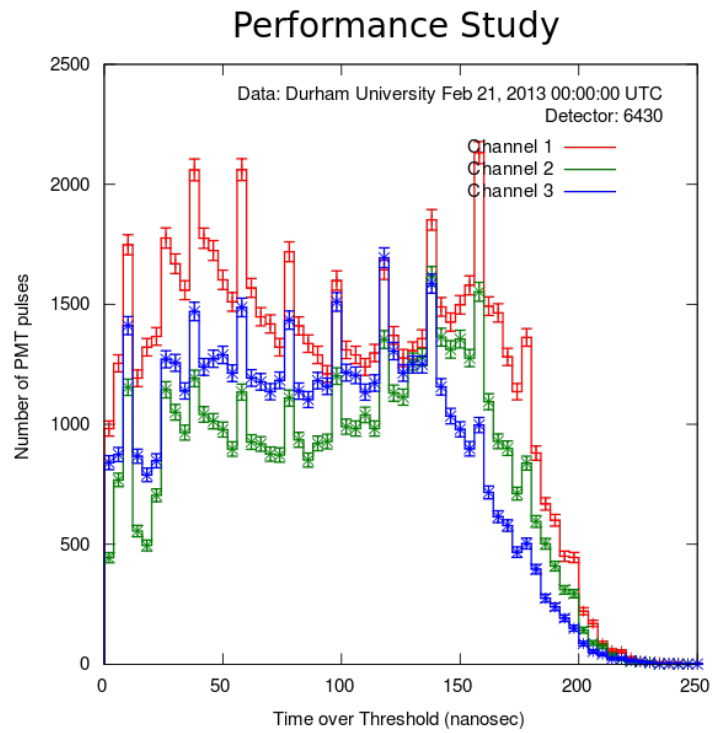
(a)
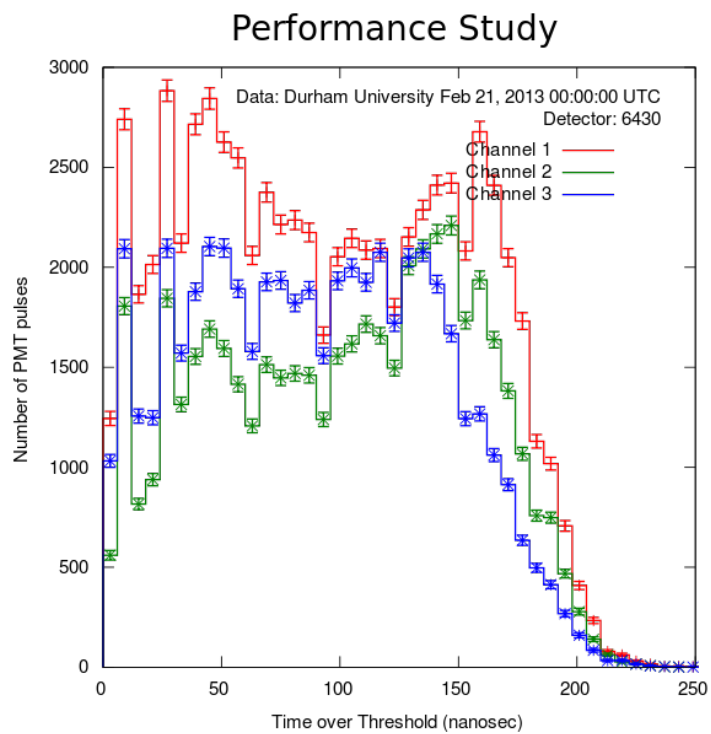
(b)

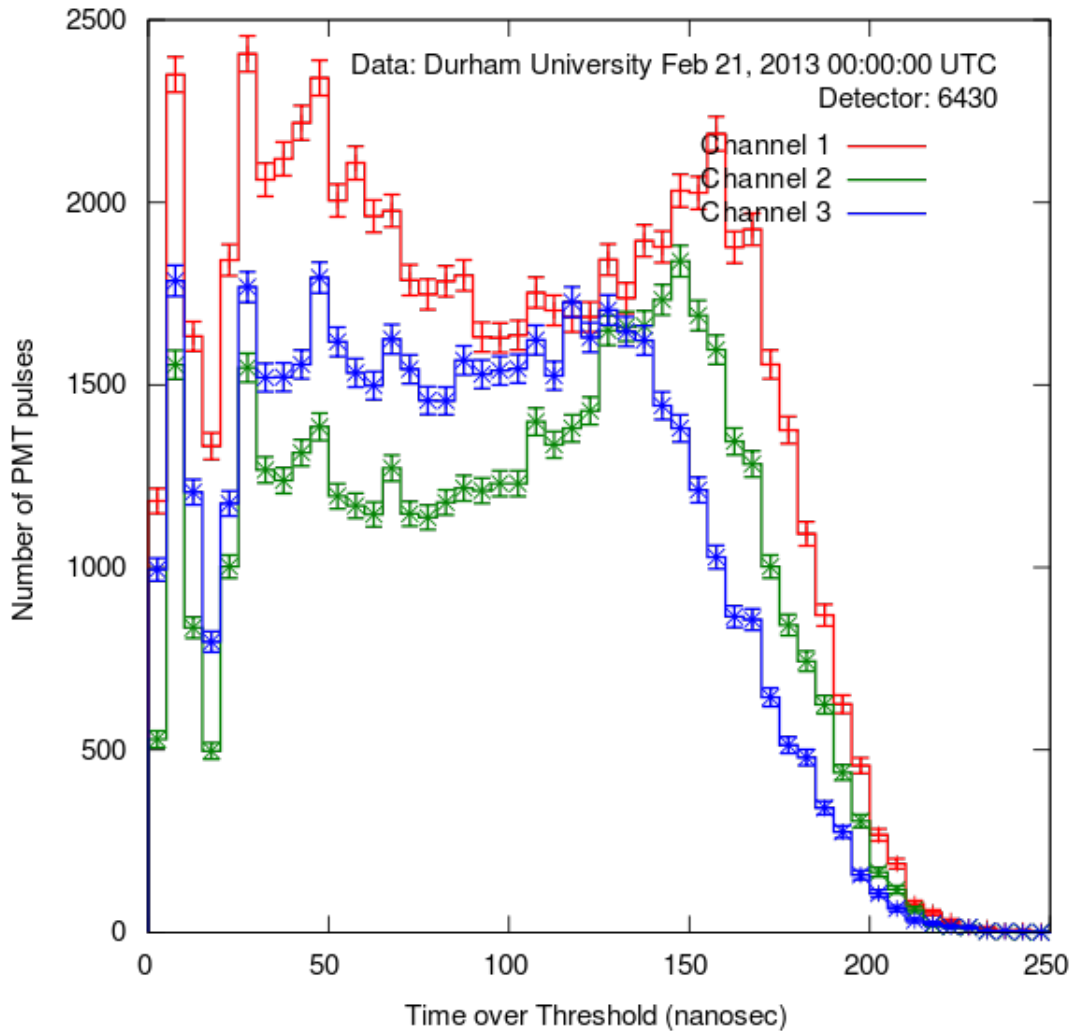Figure 4.4.5: Performance study using bin widths of 4 ns (a) and 6 ns (b).

Figure 4.4.6: Performance study on a ~24 hour data sample using a bin width of 5 ns.

As we can see in the performance plot the detector picks up a lot of noise signals. The resulting plot is far from a Gaussian distribution. The most possible explanation is that this is a fundamental issue when using the specific interface board which elongates and boosts the pulse. There is no way to know which peak corresponds to real muons passing through

the detectors and which ones correspond to noise signals.

Besides this fundamental issue the user can minimise noise levels making sure that: a) The detector box is as light-tight as possible by inserting materials like foam in the box and sealing the boxes with rubber. I tested whether the use of foam would make any difference in the noise levels and the answer is positive. For this purpose I inserted a large piece of foam inside a detector box and I observed the amplitude of noise pulses. They were (2.0±0.5) mV when there was foam and (13±2) mV when the counter operated without it. Since the muon pulses were about 10 mV with only a few exceeding up to 50 mV, we can understand the importance of the foam. Moreover, I put a rubber strip on the edges of the lid so that even fewer photons enter the box from gaps between the box and its lid. b) There is no source of ionising radiation near the detectors such as radioactive sources. During the course of these experiments there was not a source of ionising radiation in the immediate vicinity of the detectors. c) The noise resulting from malfunctioning equipment is minimised. For example, the use of a good BNC cable to connect the DAQ board to the PMTs made a difference as opposed to using a "noisy" cable.

A possible improvement is to install an ADC (analogue-to-digital converter) on the board to measure the height of the pulse and thus the energy instead of the TDC (time-to-digital converter) used now. This however will increase the cost of the detector.

4.5 Flux experiments

The next simplest experiment that can be done with the detectors is to measure the flux of muons. Different geometries of the detectors can be used for this experiment: a single detector, multiple detectors in the same plane and stacked detectors that require coincidence are some examples. Students can study the dependancy of the flux of cosmic rays on the time of day, solar activity, east/west asymmetry, angle from vertical, barometric pressure, altitude and more. These experiments are exciting for the imagination and the creativity of the students because they are able to decide what exactly they want to study. Again, data are uploaded and analysed on the cosmic ray e-lab.

Execution

The detectors remain in a stacked configuration. As in the performance experiment, a flow of data has to be recorded in a file for analysis. Therefore the same commands are typed in order to keep the information on the file: WC 02 e8 and WC 03 03, TL 4 090, V1, V2, DG, TL, WC 00 0F, ST 2 5, RB, CE. The command CD stops the flow of data.

Analysis

Two sets of data are presented here, to show how the analysis tools can be used. The first is a set data taken over 4 hours and the second over 48 hours. The user can choose the bin width to produce a plot with as much detail as required. For the first set (Fig.4.5.1-3) the bin width was set to 120 s while for the second set (Fig.4.5.4-6) it was set to 1800 s.

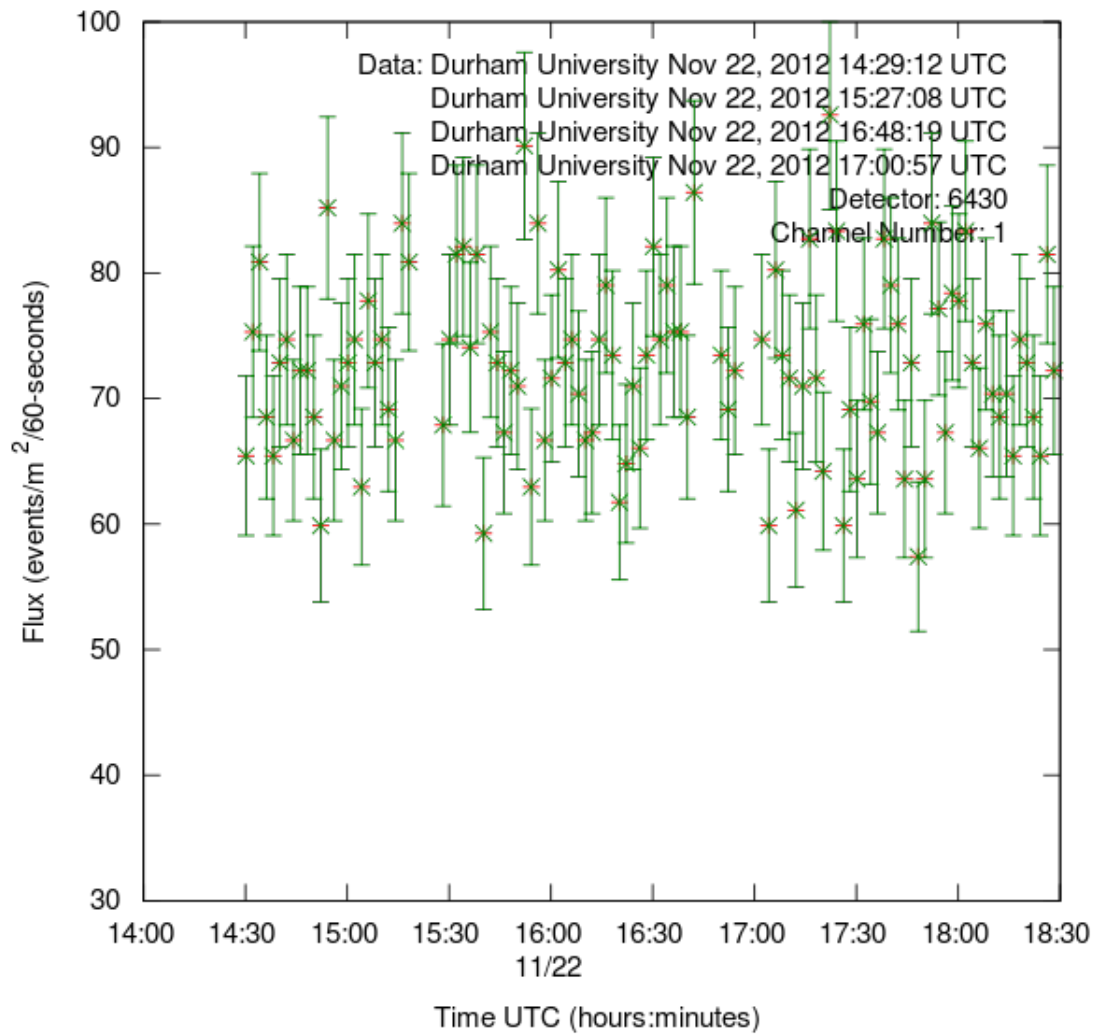Figure 4.5.1: Muon flux in the first channel during the course of 4 hours.
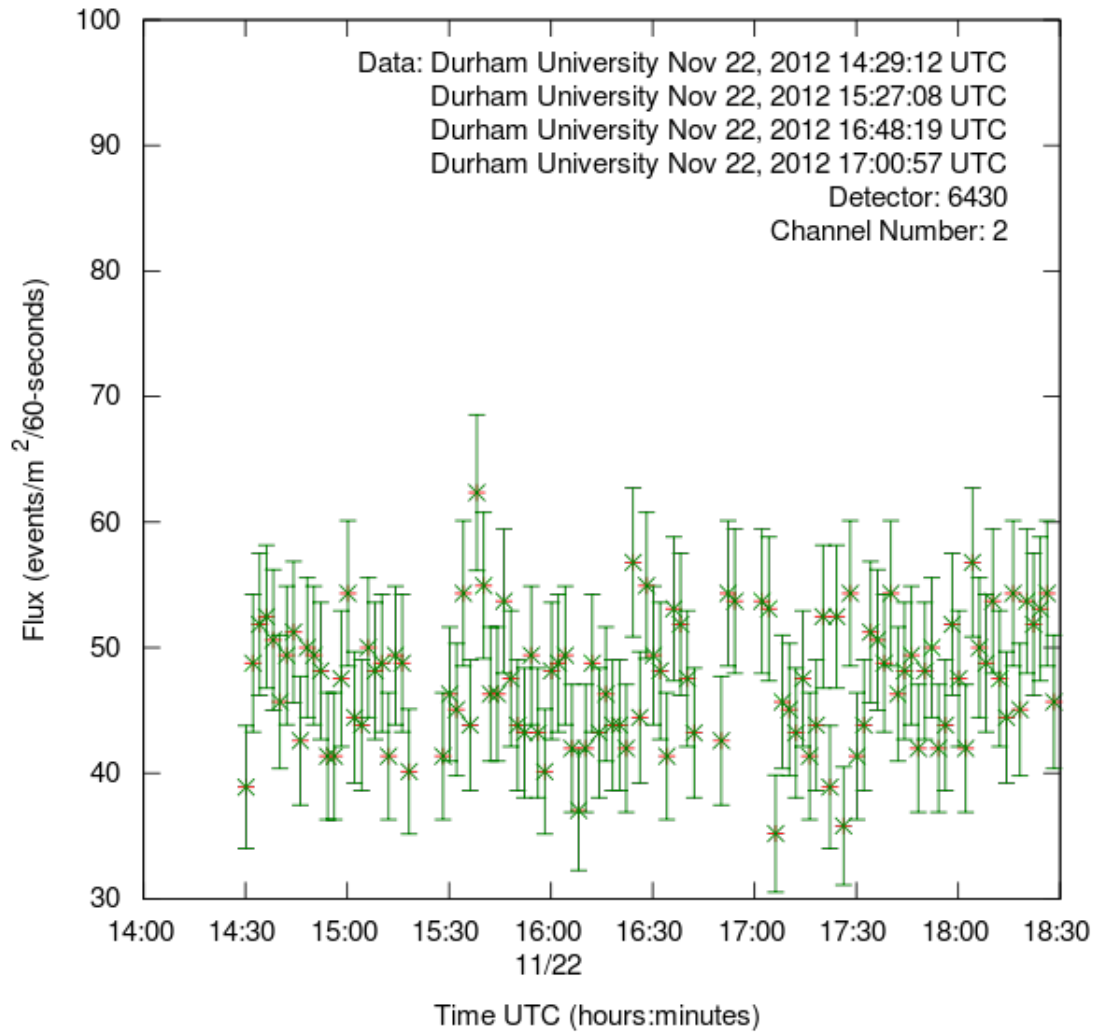
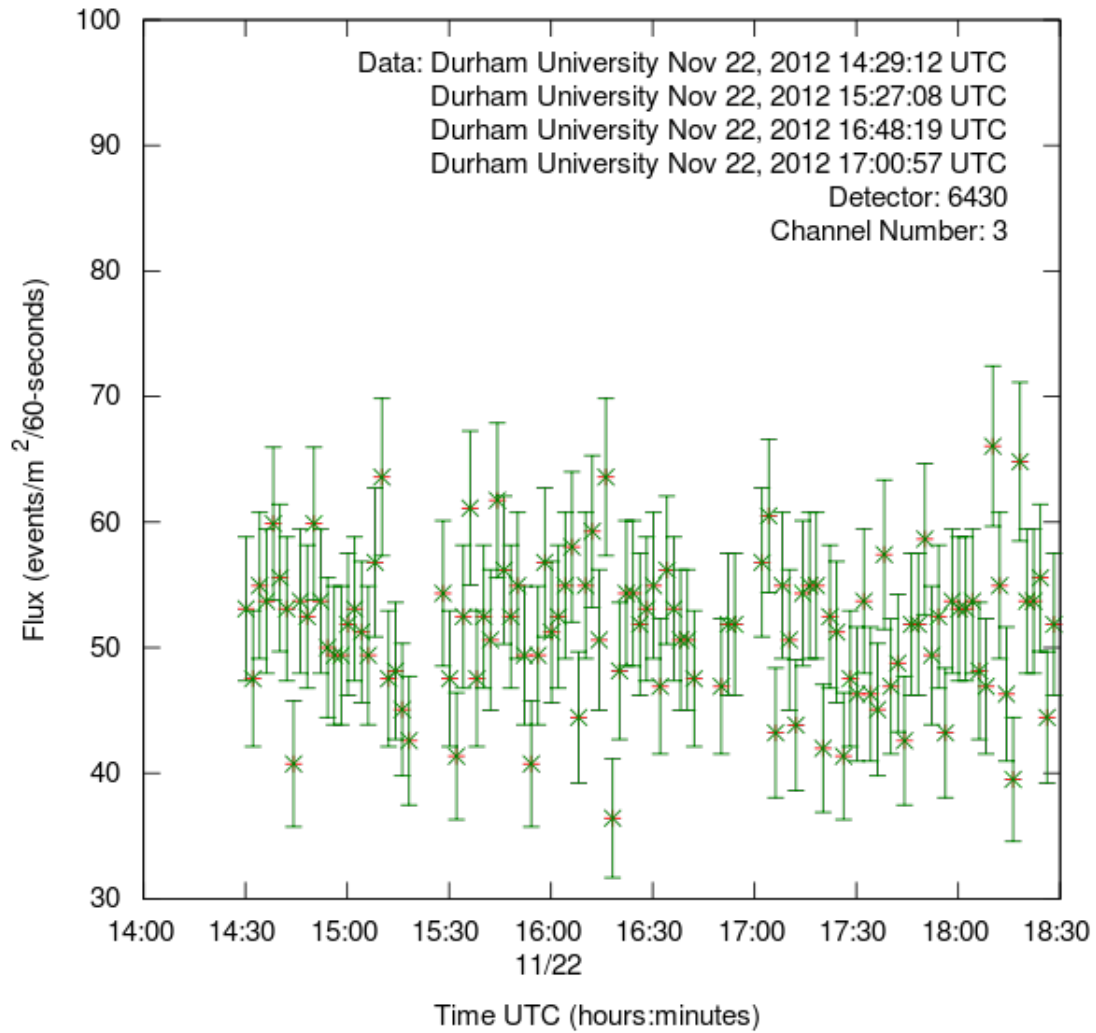Figure 4.5.2: Muon flux in the second channel during the course of 4 hours.

Figure 4.5.3: Muon flux in the third channel during the course of 4 hours.
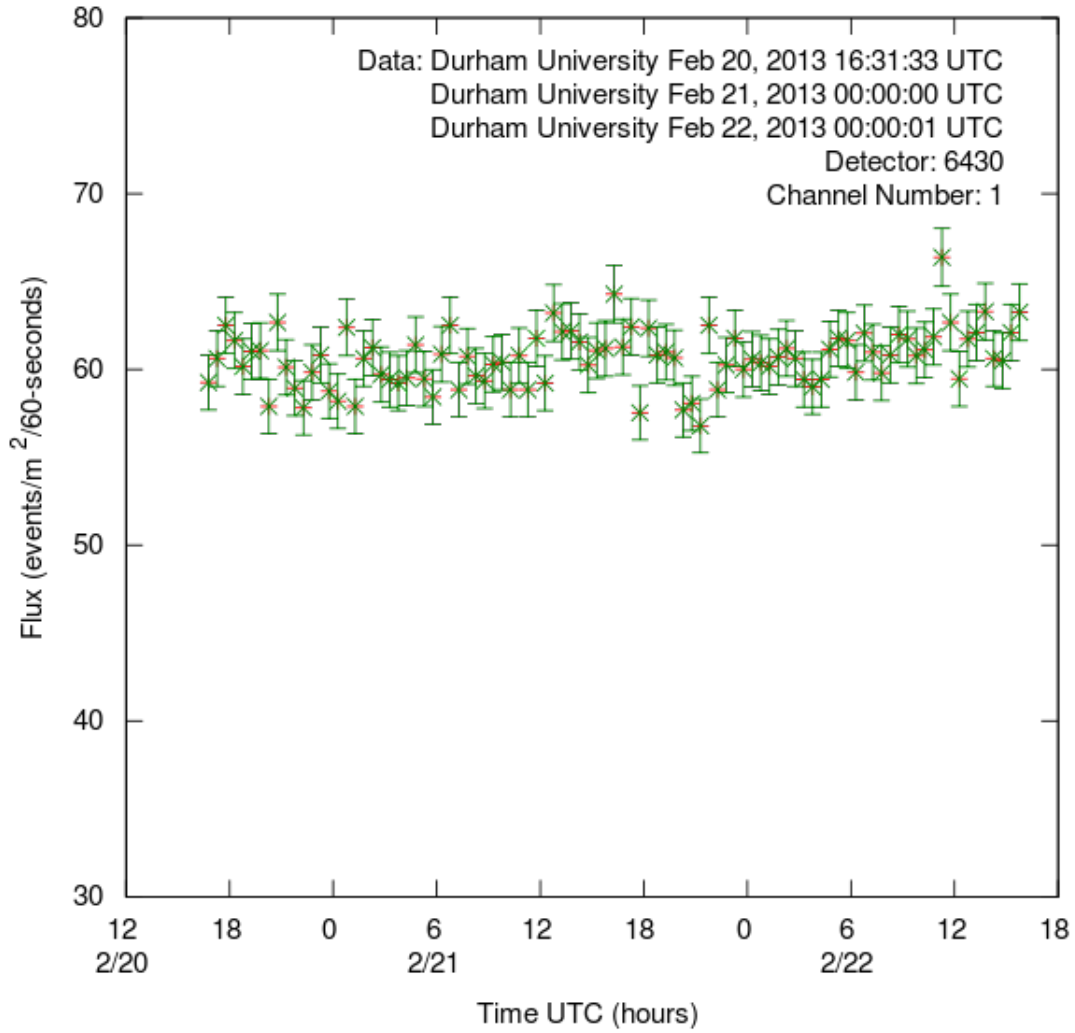
Figure 4.5.4: Muon flux in the first channel during the course of 48 hours.
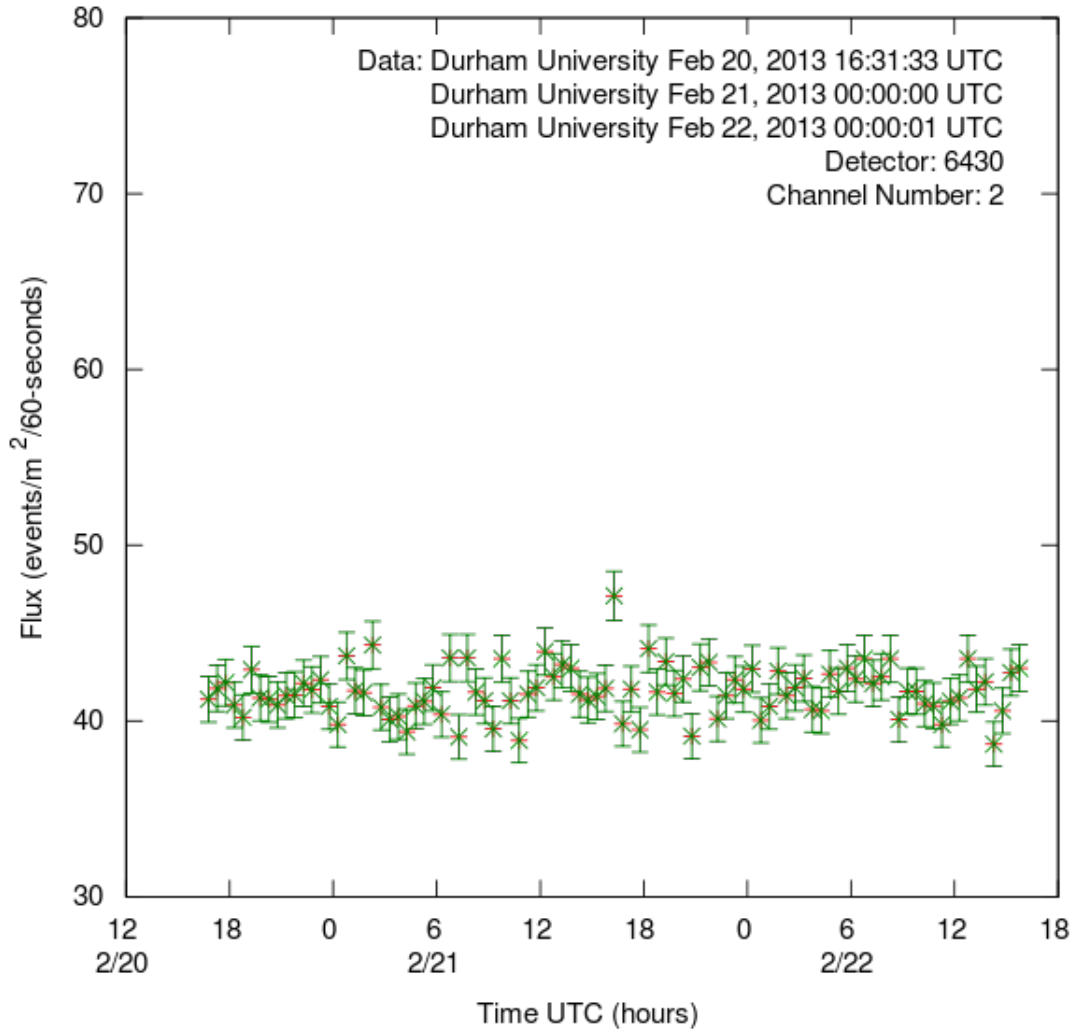
Figure 4.5.5: Muon flux in the second channel during the course of 48 hours.
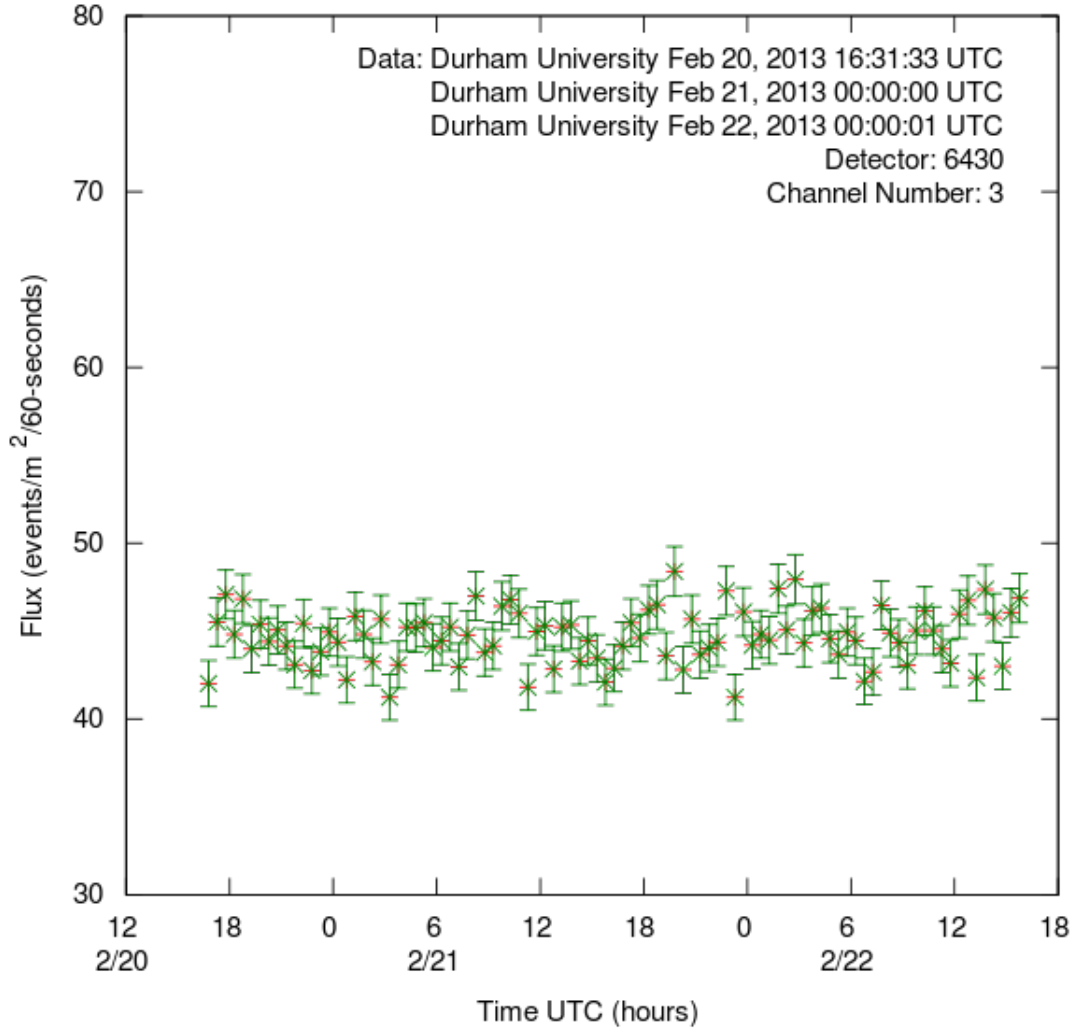
Figure 4.5.6: Muon flux in the third channel during the course of 48 hours.

For the 4-hour plots the flux is found to be $J_1 = (74 \pm 16)$ m^{-2}min^{-1}, $J_2 = (48 \pm 14)$ m^{-2}min^{-1} and $J_3 = (52 \pm 17)$ m^{-2}min^{-1} and for the 48-hour plots $J_1 = (60 \pm 3)$ m^{-2}min^{-1}, $J_2 = (42 \pm 3)$ m^{-2}min^{-1} and $J_3 = (45 \pm 4)$ m^{-2}min^{-1}. The values for each channel agree in each case. The difference in uncertainties has to do with the different width of the bin: a larger bin takes into account more measurements and the average

for each bin is more accurate.

There are three points that can be made from these plots. First, the flux measured in the first channel is slightly higher than the flux in the other two channels. This probably has to do with the fact that the first detector was equipped with the Bristol board and the procedure of finding the optimum operating voltage (plateauing) was not followed as with the Durham boards.

Second, the measured flux in all three detectors is much lower than the flux expected from theoretical calculations. In chapter 1 I calculated the flux of muons at sea level to be $J = (1.26 \pm 0.02) \times 10^{-2} \text{cm}^{-2}\text{s}^{-1} = (7560 \pm 120) \text{ m}^{-2}\text{min}^{-1}$. The flux that I measured is ~ 100 times smaller. This is due to the fact that the lowest energy muons are not detected.

In fact, the threshold muon energy measured by the detectors can be found. Assuming that all particles come in from an angle bigger than $45°$, we can calculate how many steradians are covered and the result is $\pi(2 - \sqrt{2})$. Taking an average flux value of 50 $\text{m}^{-2}\text{min}^{-1} = 0.8$ $\text{m}^{-2}\text{s}^{-1}$, and dividing it by the number of steradians we find that the flux is 0.4 $\text{m}^{-2}\text{s}^{-1}\text{sr}^{-1}$. As it can be found be comparing the measured flux to the bibliography [72], the corresponding energy is between 50 and 100 GeV. Therefore, our detectors do not count muons with energies lower than this value.

Third, the variation in the flux depends on how detailed the plots are. During the course of the 48 hours there is no significant variation observed. As mentioned, the bin width is 1800 s and the estimated values for the flux are $J_1 = (60 \pm 3) \text{ m}^{-2}\text{min}^{-1}$, $J_2 = (42 \pm 3) \text{ m}^{-2}\text{min}^{-1}$, $J_3 = (45 \pm 4) \text{ m}^{-2}\text{min}^{-1}$. This means that the relative variation is 5% for

the first and 7% for the second and 9% for the third detector which is small. On the other hand, the bin width for the 4-hour plots is 120 s and the estimated values for the flux are $J_1 = (74 \pm 16)$ m^{-2}min^{-1}, $J_2 = (48 \pm 14)$ m^{-2}min^{-1}, $J_3 = (52 \pm 17)$ m^{-2}min^{-1}, hence the variation rises to 22%, 29% and 33% respectively. To conclude, on a long time scale the muon flux is almost stable but on a smaller time scale the flux variation is larger due to statistical effects.

4.6 Muon lifetime and time dilation experiments

Muon lifetime measurement is a very interesting experiment since it can be used to prove relativistic time dilation. The basic thinking for this experiment is the following: three detectors are stacked one on top of the other. When a muon enters the top detector, a signal is generated. If the muon passes through the detector and enters the middle detector, then a second signal should be produced almost immediately after the first. If the muon stops inside that detector and decays giving an electron, then a second signal will be generated from this detector. The time between these two signals from the second detector is the decay time. The absence of signal from the bottom detector is a strong indication that the muon did indeed decay inside the middle detector.

However, my analysis only yielded results only when the coincidence level was set to 1. More details can be found in the Analysis section.

Nevertheless, the thinking behind finding the muon lifetime from our

data is the same. It can be calculated from the exponential curve that describes the phenomenon (Fig.4.6.1) where we plot the number of events versus the decay time (the lifetime).

The expression is $N(t) = N_0 \, e^{(-1/\tau)}$, with τ the mean lifetime, N_0 the total number of muons that decayed in the detector and $N(t)$ is the number of muons with lifetime longer than t. The expected muon lifetime is (2.197 ± 0.001) μs [73].
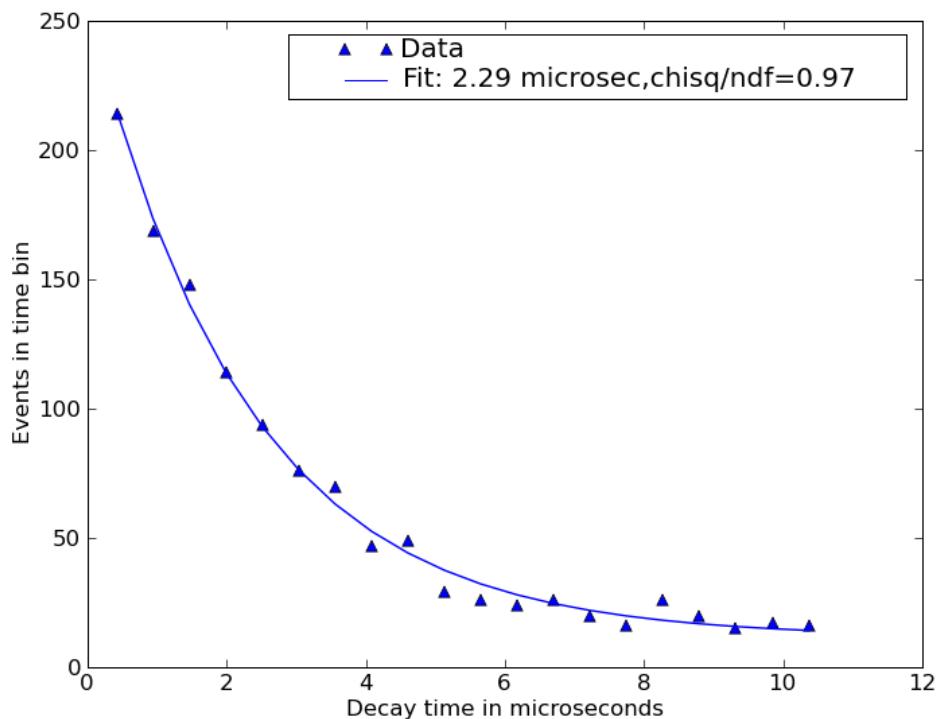

Figure 4.6.1: Example of an exponential curve showing number of decays as a function of decay time, used to calculate the muon lifetime [62].

The fact that the muon was created some time before entering the detector is not a problem because the shape of the curve and thus its parameters remain the same.

For this experiment it is important to take data in the course of 24 hours or more in order to record enough events, as muon decays are quite rare. It is essential that the detectors are stacked during the run.

Execution

The detectors were stacked and the same commands were entered at the beginning of the run: WC 02 e8 and WC 03 03, TL 4 090, V1, V2, DG, TL, WC 00 0F, ST 2 5, RB, CE and CD to stop the data. Data were taken for about 56 hours.

Analysis

The data set is uploaded to the cosmic ray e-lab website with information about the geometry if required. During the analysis there is the option to choose the coincidence level as well as the gate width. For the data analysed here the gate width had been set to 10 μs i.e. a little bigger than the expected muon lifetime because we are looking to detect the electron pulse several μs after the muon pulse. The TMC delay was set to 40 ns. This configuration, which is suggested by QuarkNet for this particular experiment, means that in order to detect a coincidence between two detectors (coincidence level 2) the two pulses should be at the most 40 ns apart. This is expected with the QuarkNet detecting system because a muon travelling with the speed of light takes only a few ns to cover the

distance between two stacked detectors. However, the present analysis does not yield the same results for the CORUS system.

The online analysis only detects decays when the coincidence level is set to 1. For any other coincidence level the result is that there are no decays although the DAQ board counter shows that there are. Therefore the analysis tool fails to recognise the coincidences between two or three detectors. Nevertheless, the result is close to the true value.

Setting the coincidence to 1 gives the plots of Figures 4.6.2 and 4.6.3 using different number of bins in each. The number of bins that is chosen depends on the quality and quantity of the data. The fitting should also be turned on so that the online analysis gives the best-fitting curve and its parameters. In Figure 4.6.2 where 10 bins are used there is almost no bin with zero elements and the result is as close to the true value as it can get with any number of bins which makes the 10 bins the best choice. In Figure 4.6.3, where 50 bins are used, although there is the smallest error that could be achieved, the value of the lifetime is less close to the true value and also there are many bins with zero elements. The result of (2.3±0.6) μs is in very good agreement with the expected value (2.2 μs).
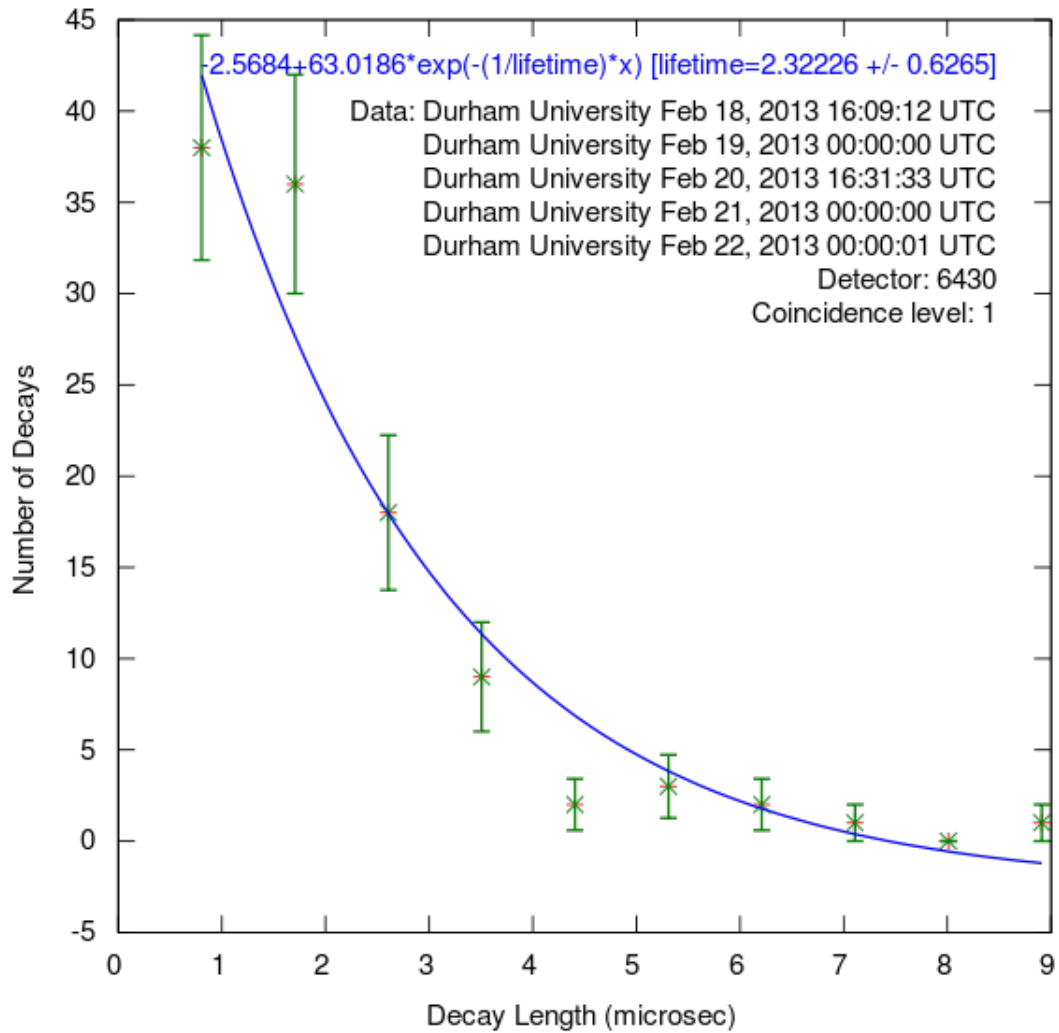
Figure 4.6.2: Muon lifetime analysis taken over the course of about 56 hours. The result is in good agreement with the true value of the lifetime of a muon (2.2 μs). Coincidence=1, bins=10, gate width=10 μs.
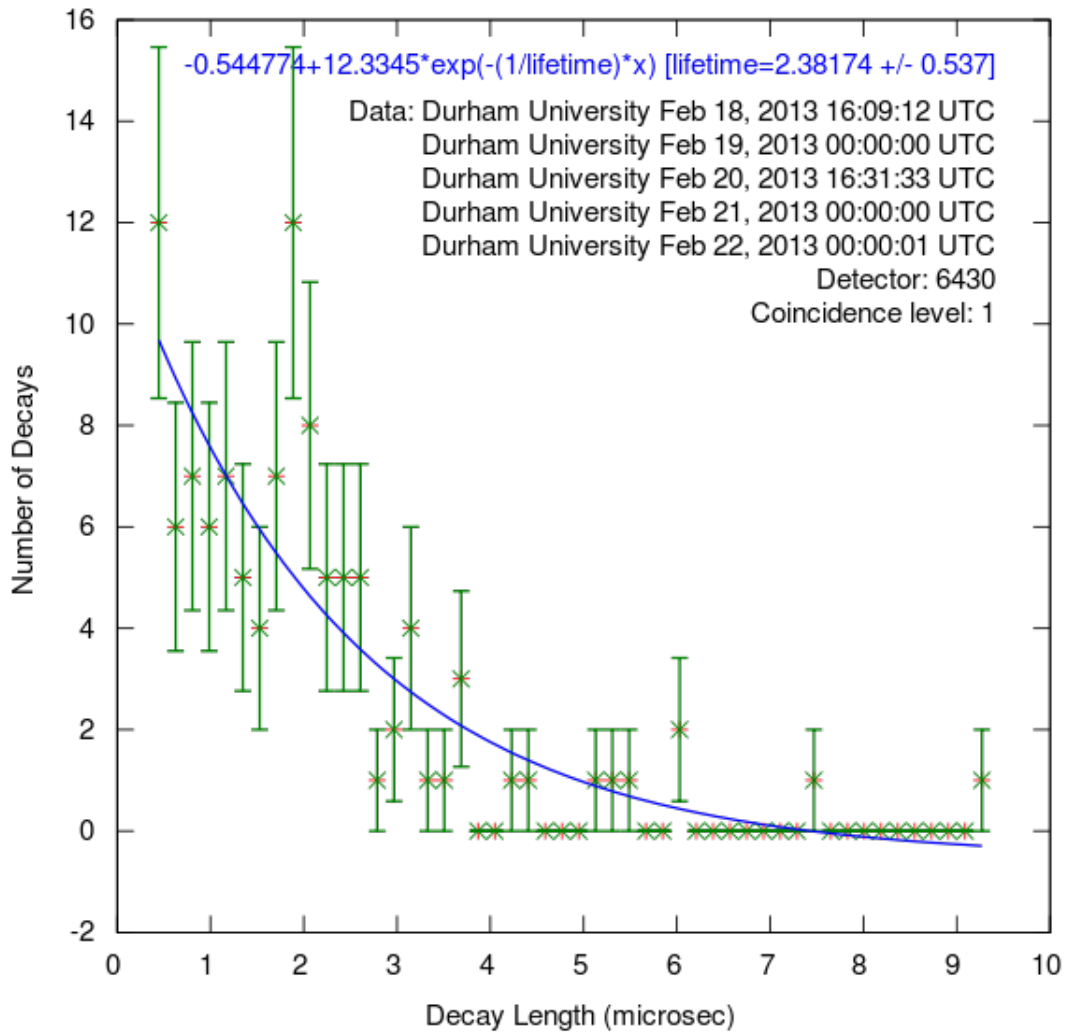
Figure 4.6.3: Muon lifetime analysis taken over the course of about 56 hours. Coincidence=1, bins=50, gate width=10 μs.

As mentioned, students can prove relativistic time dilation. We know that muons are created in the upper atmosphere (about 30 km above the surface of the earth) and we can assume that they travel with the speed of light (3×10^8 m/sec) therefore we can calculate the time they need to reach our detectors:

$$t = \frac{d}{v} = \frac{30 \times 10^3}{3 \times 10^8} = 100 \ \mu s \qquad (4.6.1)$$

This number is much bigger than the muon lifetime so we would expect all muons to have decayed before they reach the ground although clearly this is not the case. The answer to this contradiction is found using Special Relativity and the concept of time dilation. In the reference frame of the observer, i.e. us, time is dilated as follows:

$$t = \frac{t_0}{\sqrt{1 - \frac{v^2}{c^2}}} \qquad (4.6.2)$$

where t_0 is the lifetime in the rest frame of the muon, v its velocity and c the speed of light. Muons travel at 99.9985% of the speed of light so the above formula gives t=415 μs for the lifetime of a muon in the reference frame of an observer on earth. This calculation explains why we are able to detect muons on the surface of the earth and it is a very nice and intriguing way to introduce some concepts of Special Relativity to students.

4.7 Shower studies

The GPS device allows a network of detectors to be built. Students can look for small showers over their own detectors or different schools can compare their data through the web to reconstruct cosmic ray showers and determine the direction of the shower (and thus the primary cosmic ray).
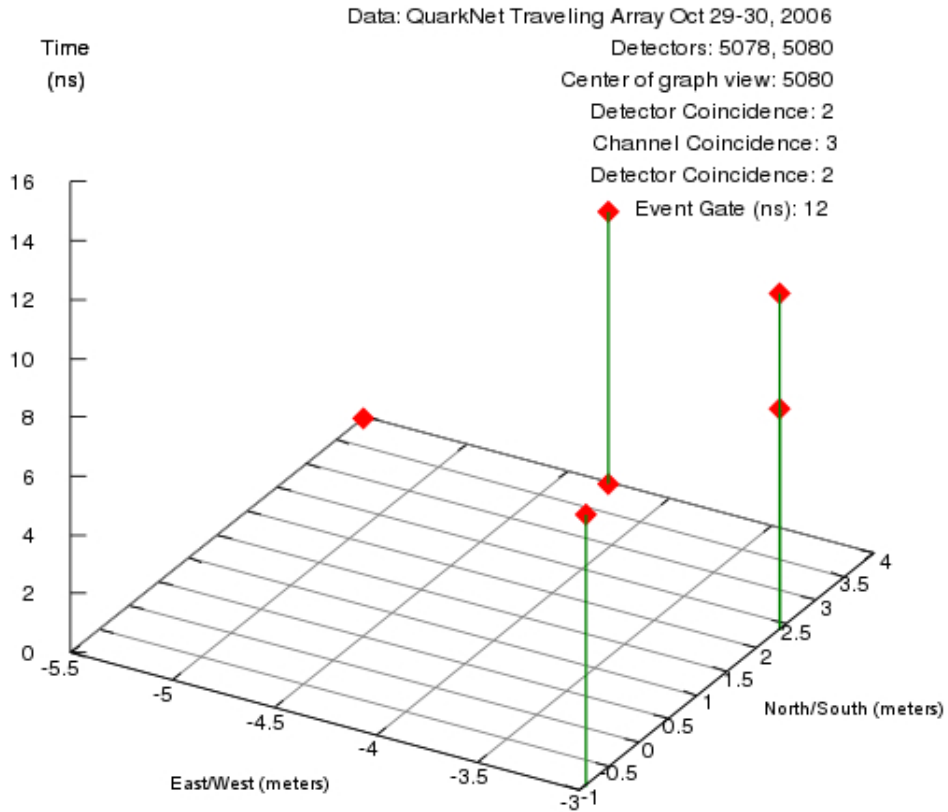
The muons produced in an air shower will spread out as they travel towards the ground but they will arrive at sea level within about 100 ns of each other. The size of the air shower and the number of particles are determined by the energy of the primary cosmic ray. The highest energy primary cosmic rays produce large air showers which can extend up to several km^2.

A school using the QuarkNet system can measure small, local showers by spreading out the detectors on a plane, covering an area of about 0.5 m^2 and setting the gate width to 100 ns, the TMC delay to 40 ns and coincidence to 1. This way the single delayed pulses in each channel will be read out. The analysis gate width which is set online must again be set to 100 ns, the coincidence of channels and events is set accordingly to the detector set up each school has. The former means how many detectors should be hit for a coincidence and the latter how many signals should be detected among the 4 counters. The detector coincidence is set normally to 1 (this means how many schools are participating). The online analysis will detect all pulses in different channels within a 100 ns window as a shower event. Moreover, different schools in the same town can cooperate and record data at the same time, thus being able to "see"

larger showers.

The online analysis gives a lists of candidate shower events and the number of events (signals) in each one. Specific showers can then be plotted on a 3-D graph (Fig.4.7.1). The x and y axes correspond to the position of the detector i.e. the signal in relation to the GPS antenna and the values are inputted in the system before the analysis. The z axis corresponds to the time the signal was detected. A list of all the events in the shower is also provided. The direction of the shower can be determined by locating the first particle that was detected. In this case the shower originated from the Northwest.

Figure 4.7.1: Example of a 3-D shower plot which can be found at the cosmic ray e-lab. Below the plot there is a list of the events with position and time of each event. In this case, the shower originated from the Northwest [60].

In order to detect showers with CORUS the working principles are the same. The detectors are spread on a plane and the geometry is uploaded on the e-lab. The only difference between the QuarkNet and the CORUS system that is important for this experiment is the elongated pulse of CORUS which is 200 ns. Therefore, the gate width must be set to at least 300 ns if the TMC delay is 40 ns, for our detectors to be able to read out the leading and trailing edges of the delayed pulse of each single pulse. The settings of the online analysis are the same except for the gate width which must be again 300 ns. As with QuarkNet, all pulses coming in 100 ns after the first are considered a shower. The larger gate width serves just to be able to detect the trailing edges of the pulses within a 100 ns window. The reconstruction of the shower is done by the e-lab analysis tool the same way as in QuarkNet. A 3-D plot similar to that of Figure 4.7.1 should be produced so that the shower direction can be determined.

To conclude, there is no reason why the CORUS detecting system cannot yield good results on the shower detection experiment. This hypothesis has still to be proved by taking a 24-hour long data set and analysing it online.

4.8   Commands catalogue

command	description	use
TL c d	Threshold Level, c is the channel (0-3, 4=all channels), d=voltage (0-4095 mV)	sets the threshold voltage
TL	Threshold Level	prints the threshold level
WC 00 nm	Write Control registers, n sets a n+1 coincidence, m is hexadecimal number of channels that are enabled	sets the coincidence and enabled desired counters
WC 02 ab WC 03 cd	Write Control registers, ab cd is the hexadecimal number of clock ticks required for the gate width (1 clock tick is 10 ns)	sets the gate width
V1, V2	View registers	prints registers is readable form
DG	Display GPS	prints GPS info, date, time, position, status
ST 2 m	STatus, m is the number of minutes	prints a status line necessary for the file to be read by the online analysis tool
RB	Reset Board	resets TMC and counters
CE	Counter Enable	starts the flow of data
CD	Counter disable	stops the flow of data
H1, H2	Help	prints all the available commands

4.9   Conclusions

I presented the basic experiments that are studied by the QuarkNet schools and institutes and my experience when I tried to reproduce them with the detectors designed for CORUS.

There are technical issues that need to be taken into account and if possible to be resolved:

1. The detectors pick up a lot of noise. In order to minimise this, they have to be as light-tight as possible, and taking into account the noise levels I detected, simply inserting foam and pond liner in the box is not enough. Moreover, our time resolution might not be good enough and this might be a fundamental issue with the elongated pulses.

2. The old ZEUS PMTs can lead to variable results for each detector. Perhaps new PMTs will minimise this effect.

3. Moreover, the interface board creates some problems of variability between detectors and it may also be responsible for some of the noise. If they are used it is preferable to be manufactured by the same producer in order to be identical.

4. The main difference between QuarkNet and CORUS is the length of the signal. The interface boards connected to the ZEUS PMTs elongates the pulse up to 200 ns and therefore some adjustments to the settings are needed.

5. The e-lab analysis tool does not yield results for the muon lifetime

experiment when coincidence level is set to 2 or 3. This has to be explained and corrected.

In conclusion, these detectors can serve as the basic design used in CORUS since they are a low cost and safe system. As I demonstrated the CORUS detectors are able to perform every experiment that can be conducted with the QuarkNet detectors and the differences between the two systems don't impose any limitations. The successful measurement of the muon lifetime is a strong proof. With some improvements of the individual components, as discussed throughout this study, these detectors are the right tools to be used by the schools participating in the CORUS project. Thus, the construction of a school network dedicated to studying cosmic rays is possible.

Bibliography

[1] V.F. Hess, *Über Beobachtungen der durchdringenden Strahlung bei sieben Freiballonfahrten*, Physikalische Zeitschrift, vol. 13, p. 1084-1091, 1912

[2] T.K. Gaisser, *Cosmic ray and particle physics*, Cambridge University Press, 1990

[3] P.K.F. Grieder, *Cosmic rays at Earth*, Elsevier, 2001

[4] M.M. Shapiro, R. Silderberg, J.P. Wefel, *Proceedings of the NATO advanced study institude on cosmic rays, supernovae and the interstellar medium*, Kluwer Academic Publishers, 1990

[5] K. Greisen, *End to the cosmic-ray spectrum?*, Physical Review Letters, vol. 16, p. 748-750, 1966

[6] G.T. Zatsepin, V.A. Kuzmin, Pis'ma v Zh. Eksp. Teor. Fiz., vol. 4, p. 114, 1966

[7] Pierre Auger Collabotation, *Measurement of the energy spectrum of cosmic rays above 10^{18} eV using the Pierre Auger Observatory*, Physics Letters B, vol. 685, p. 239-246, 2010

[8] S.P. Swordy, *The energy spectra and anisotropies of cosmic rays*, Space Science Reviews, vol. 99, p. 85-94, 2001

[9] www.physics.utah.edu/∼whanlon/spectrum.html, May 2012

[10] E. Waxman, *Cosmological gamma-ray bursts and the highest energy cosmic rays*, Physical Review Letters, vol. 75, p. 386-389, 1995

[11] M. Vietri, *On the acceleration of ultra high energy cosmic rays in gamma ray bursts*, Astrophysical Journal, vol. 453, p. 883-889, 1995

[12] M. Milgrom, V. Usov, *Possible association of ultra-high-energy cosmic-ray events with strong gamma-ray bursts*, Astrophysical Journal Letters, vol. 449, L37, 1995

[13] E.G. Berezhko, *Cosmic rays form active galactic nuclei*, Astrophysical Journal Letters, vol. 684, L69-L71, 2008

[14] N. Armesto, M.A. Braun, E.G. Ferreiro, C. Pajares, Yu. M. Shabelski, *Fusion of strings and cosmic rays at ultrahigh energies*, Physics Letters B, vol. 389, p. 78-82, 1996

[15] A.M. Hillas, *The origin of ultra-high-energy cosmic rays*, Annual Review of Astronomy and Astrophysics, vol. 22, p. 425-444, 1984

[16] J. Wdowczyk, A.W. Wolfendale, *Highest energy cosmic rays*, Annual Review of Nuclear and Particle Science, vol. 39, p. 43-71, 1989

[17] C. Amsler et al., *Cosmic rays*, Physics Letters B, vol. 667, p. 254-260, 2008

[18] O.C. Allkofer, University of Kiel, Internal report, 1965

[19] P. Budini, G. Molière, *in Kosmische Strahlung*, Springer, 1953

[20] K.I. Greisen, *The intensities of the hard and soft components of cosmic ryas as functions of altitude and zenith angle*, Physical Review, vol. 61, p. 212-221, 1942

[21] J.N. Crookes, B.C. Rastin, *An investigation of the absolute intensity of muons at sea-level*, Nuclear Physics B, vol. 39, p. 493-508, 1972

[22] H.A. Bethe, *Quantenmechanik der Ein- und Zweielectronenprobleme*, Handbuch der Physik, vol. 24-1, p. 518, 1933

[23] H.A. Bethe, W. Heitler, *On the stopping of fast particles and on the creation of positive electrons*, Proceedings of the Royal Society A, vol. 146, p. 83, 1934

[24] B. Rossi, K. Greisen, *Cosmic-ray theory*, Reviews of Modern Physics, vol. 13, p. 240-309, 1941

[25] B. Rossi, *High energy particles*, Prentice-Hall, Inc., Englewood Cliffs, New Jersey, 1952

[26] J.J. Barnett et al., *Review of particle physics*, Physical Review D, vol. 54, p. 1-708, 1996

[27] U. Fano, *Penetration of protons, alpha particles and mesons*, Annual Reviews of Nuclear and Particle Science, vol. 13, p. 1-66, 1963

[28] A. Crispin, G.N. Fowler, *Density effect in the ionisation energy loss of fast charged particles in matter*, Reviews of Modern Physics, vol. 42, p. 290-316, 1970

107

[29] R.M. Sternheimer, *Density effect for the ionisation loss of charged particles in various substances*, Atomic Data and Nuclear Data Tables, vol. 30, p. 261-271, 1984

[30] M. Takeda et al., *Extension of the cosmic-ray energy spectrum beyond the predicted GZK cutoff*, Physical Review Letters, vol. 81, p. 1163-1166, 1998

[31] High Resolution Fly's Eye Collaboration, *First observation of the GZK suppression*, Physical Review Letters, vol. 100, p. 101101-101106, 2008

[32] V.P. Egorova et al., *The spectrum features of UHECRs below and surrounding GZK*, Nuclear Physics B - Proceedings Supplements, vol. 136, p. 3-11, 2004

[33] J. Lozano-Bahilo for the Pierre Auger Collaboration, *Results of the Pierre Auger observatory on high energy cosmic rays*, Journal of Physics: Conference Series, vol. 160, 012038, 2009

[34] R. Aloisio et al., *A dip in the UHECR spectrum and the transition from galactic to extragalactic cosmic rays*, Astroparticle Physics, vol. 27, p. 76-91, 2007

[35] http://www-akeno.icrr.u-tokyo.ac.jp/AGASA/, December 2012

[36] N. Hayashida et al., *Observation of a very energetic cosmic ray well beyond the predicted 2.7 K cutoff in the primary energy spectrum*, Physical Review Letters, vol. 73, p. 3491-3494, 1994

[37] M. Takeda et al., *Small-scale anisotropy of cosmic rays above 10^{19} eV observed with the Akeno Giant Air Shower Array*, Astrophysical Journal, vol. 522, p. 225-237, 1999

[38] N. Hayashida et al., *The anisotropy of cosmic ray arrival directions around 10^{18} eV*, Astroparticle Physics, vol. 10, p. 303-311, 1999

[39] J.N. Matthews for the High resolution Fly's Eye Collaboration, *Description of the High Resolution Fly's Eye detector*, Proceedings of ICRC 2001:350,

[40] High Resolution Fly's Eye Collaboration, *Search for correlations between HiRes stereo events and active galactic nuclei*, Astroparticle Physics, vol. 30, p. 175-179, 2008

[41] High Resolution Fly's Eye Collaboration, *Analysis of large-scale anisotropy of ultra-high energy cosmic rays in Hires data*, Astrophysical Journal Letters, vol. 713, L64-L68, 2010

[42] http://eas.ysn.ru, December 2012

[43] S.P. Knurenko, A.A. Ivanov, A.V. Sabourov, I.Ye. Sleptsov, *Average mass composition of primary cosmic rays in the super high energy region by Yakutsk complex EAS array data*, Proceedings of the 30th International Cosmic Ray Conference, vol. 4, p. 167-170, 2008

[44] A.A. Ivanov, *Galactic cosmic rays at 10^{19} eV*, Journal of Physics G: Nuclear and Particle Physics, vol. 24, p. 227-234, 1998

[45] V.P. Egorova et al., Journal of the Physical Society of Japan, vol. 70 (supplement B), p. 9-14, 2001

[46] http://www.auger.org, December 2012

[47] Pierre Auger Collaboration, *The fluorescence detector of the Pierre Auger Observatory*, Nuclear Instruments and Methods A, vol. 620, p. 227-251, 2010

[48] http://www.interactions.org, February 2012

[49] Pierre Auger Collaboration, *Upper limit on the cosmic ray photon flux above 10^{19} eV using the surface detector of the Pierre Auger Observatory*, Astroparticle Physics, vol. 29, p. 243-256, 2008

[50] Pierre Auger Collaboration, *Upper limit on the diffuse flux of ultrahigh energy tau neutrinos from the Pierre Auger Observatory*, Physical review Letters, vol. 100, 211101, 2008

[51] N. Hayashida et al., *The anisotropy of cosmic ray arrival directions around 10^{18} eV*, Astroparticle Physics, vol. 10, p. 303-311, 1999

[52] J.A. Bellido et al., *Southern hemisphere observations of a 10^{18} eV cosmic ray source near the direction of the Galactic centre*, Astroparticle Physics, vol. 15, p. 167-175, 2001

[53] Pierre Auger Collaboration, *Anisotropy studies around the galactic centre at EeV energies with the Auger Observatory*, Astroparticle Physics, vol. 27, p. 244-253, 2007

[54] Pierre Auger Collaboration, *Correlation of the highest energy cosmic rays with nearby extragalactic objects*, Science, vol. 318, p. 938-943, 2007

[55] Pierre Auger Collaboration, *Update on the correlation of the highest energy cosmic rays with nearby extragalactic matter*, Astroparticle Physics, vol. 34, p. 314-326, 2010

[56] Pierre Auger Collaboration, *Large scale distribution of arrival directions of cosmic rays detected above 10^{18} eV*, Astrophysical Journal Supplement Series, vol. 203, 34, 2012

[57] http://www.hisparc.nl, March 2013

[58] C. Timmermans for the HiSPARC Collaboration, *Setup and first results of the HiSPARC experiment*, Proceedings of the 29th International Cosmic Ray Conference, vol. 6, p. 345-348, 2005

[59] Loran de Vries, *Search for a correlation between HiSPARC cosmic ray data and weather measurements*, Master thesis, 2012

[60] http://www.i2u2.org/elab/cosmic/home/project.jsp, February 2012

[61] http://quarknet.fnal.gov, March 2013

[62] J. Rylander, T. Jordan, J. Pasche, R.J. Wilkes, H. Berns, R. Gran, S. Hansen, T. Kiper, *QuarkNet cosmic ray muon detector user's manual series "6000" DAQ*, Version 1.1, 2010

[63] Royal Society State of the Nation report 2011, http://royalsociety.org/education/policy/state-of-nation/higher-education/

[64] Osborne, J. and Dillon, J., Science Education in Europe: Critical Reflections, a report to the Nuffield Foundation 2008, http://www.nuffieldfoundation.org/science-education-europe

[65] http://www.iop.org/news/11/july/page_51502.html

[66] Science and Mathematics Education for the 21st Century report of the Science and Learning Expert Group, http://interactive.bis.gov.uk/scienceandsociety/site/learning/files/2010/02/Science-and-Learning-Expert-Group-Report-Annexes-31.pdf

[67] http://www.detectors.saint-gobain.com, May 2013

[68] www.hamamatsu.com, February 2013

[69] B. Lu, L.W. Mo, T.A. Nunamaker, *The Cockroft-Walton Photomultiplier tube base and the ethernet high voltage controller*, Nuclear Instruments and Methods in Physics Research Section A: Accelerators, Spectrometers, Detectors and Associated Equipment, vol. 313, p. 135-141, 1992

[70] http://en.wikipedia.org/wiki/Cockcroft_Walton_generator, May 2013

[71] D. Balick, *QuarkNet cosmic ray detection system manual*, Version 1.0, 2001

[72] http://www.kayelaby.npl.co.uk/general_physics/2_7/2_7_7.html, May 2013

[73] E. Segre, *Nuclei and particles*, W.A. Benjamin, Inc., 1965